Microscopic pK_a Analysis of Glu286 in Cytochrome *c* Oxidase (*Rhodobacter sphaeroides*): Toward a Calibrated Molecular Model[†]

Nilanjan Ghosh,[‡] Xavier Prat-Resina,[‡] M. R. Gunner,[§] and Qiang Cui*[,‡]

Department of Chemistry, University of Wisconsin, 1101 University Avenue, Madison, Wisconsin 53706, and Department of Physics, City University of New York, 138th Street and Convent Avenue, New York, New York 10031

Received November 18, 2008; Revised Manuscript Received January 6, 2009

ABSTRACT: As stringent tests for the molecular model and computational protocol, microscopic pK_a calculations are performed for the key residue, Glu286, in cytochrome *c* oxidase (CcO) using a combined quantum mechanical/molecular mechanical (QM/MM) potential and a thermodynamic integration protocol. The impact of the number of water molecules in the hydrophobic cavity and protonation state of several key residues (e.g., His334, Cu_B-bound water, and PRD_{a3}) on the computed microscopic pK_a values of Glu286 has been systematically examined. To help evaluate the systematic errors in the QM/MM-based protocol, microscopic pK_a calculations have also been carried out for sites in a soluble protein (Asp70 in T4 lysozyme) and a better-characterized membrane protein (Asp85 in bacteriorhodopsin). Overall, the results show a significant degree of internal consistency and reproducibility that support the effectiveness of the computational framework. Although the number of water molecules in the hydrophobic cavity does not greatly influence the computed pK_a of Glu286, the protonation states of several residues, some of which are rather far away, have more significant impacts. Adopting the standard protonation state for all titratable residues leaves a large net charge on the system and a significantly elevated pK_a for Glu286, highlighting that any attempt to address the energetics of proton transfers in CcO at a microscopic level should carefully select the protonation state of residues, even those not in the immediate neighborhood of the active site. The calculations indirectly argue against the deprotonation of His334 for the proton pumping process, although further studies that explicitly compute its pK_a are required for a more conclusive statement. Finally, the deprotonated Glu286 is found to be in a stable water-mediated connection with PRD_{a3} for at least several nanoseconds when this presumed pumping site is protonated. This does not support the proposed role of Glu286 as a robust gating valve that prevents proton leakage, although a conclusive statement awaits a more elaborate characterization of the Glu286−PRD_{a3} connectivity with free energy simulations and a protonated PRD_{a3}. The large sets of microscopic simulations performed here have provided useful guidance to the establishment of a meaningful molecular model and effective computational protocol for explicitly analyzing the proton transfer kinetics in CcO, which is required for answering key questions regarding the pumping function of this fascinating and complex system.

One of the key challenges of molecular bioenergetics is to understand the function and mechanism of membrane-bound ion pumps in structural and energetic terms. One of the most fascinating systems in this context is cytochrome *c* oxidase (CcO),[1] which is a complex, multisubunit heme-copper oxidase and the terminal enzyme of the electron transfer pathway in cellular respiration. It activates the kinetically stable oxygen molecule to prevent the release of potentially toxic oxygen intermediates and, at the same time, uses the free energy from oxygen reduction to pump protons across the mitochondrial membrane in a stochiometric fashion, creating the proton concentration gradient required for ATP synthesis (*1*−*5*). For each reduced oxygen molecule, four electrons and four (substrate) protons are consumed in the oxygen reduction process while four other (pumped) protons are pumped across the membrane. It is generally believed that the electron transfer, proton consumption, and proton pumping are carefully orchestrated by CcO to achieve a tight coupling between the oxygen reduction and proton pumping. The precise mechanistic details of the coupling process, however, have largely remained obscure, making CcO a current topic of intense research.

With the recent advances in the structural characterization of CcO in different redox states (*6, 7*), it has become feasible to carry out theoretical and computational studies on the detailed proton pumping mechanism in this complex system. A series of electrostatic (*8*−*12*), classical molecular dynamics simulations (*13*−*16*), and quantum chemical study of active

[†] These studies were partially supported by the National Science Foundation (CHE-CAREER-0348649 to Q.C. and MCB-0517589 to M.R.G.). Q.C. acknowledges a Research Fellowship from the Alfred P. Sloan Foundation.

* To whom correspondence should be addressed. E-mail: cui@chem.wisc.edu. Phone: (608) 262-9801. Fax: (608) 262-9918.

[‡] University of Wisconsin.

[§] City University of New York.

[1] Abbreviations: CcO, cytochrome *c* oxidase; bR, bacteriorhodopsin; MCCE, multiconformer continuum electrostatics; GSBP, generalized solvent boundary potential; GCMC, grand canonical Monte Carlo; QM/MM, quantum mechanical/molecular mechanical; SCC-DFTB, self-consistent charge-density functional tight binding; TI, thermodynamic integration; BNC, binuclear center; PLS, proton loading site.

10.1021/bi8021284 CCC: $40.75
Published on Web 02/25/2009

site models (*17*−*19*) have already provided interesting insights into various mechanistic issues. Nevertheless, fundamental issues such as the precise identity of the pumped proton loading site(s) and the gating mechanism of substrate versus pumped proton transfers have not been firmly resolved. Our long-term goal is to make contributions to solving these key mechanistic issues using combined quantum mechanical/molecular mechanical (QM/MM) calculations. We believe that QM/MM calculations are particularly useful in this context because both proton transfer thermodynamics and kinetics (barriers) can be addressed on an equal footing within such a computational framework. With regard to CcO, it is important to explicitly estimate the proton transfer kinetics since a number of authors (*20*−*22*), including us, have argued that the phenomenon of "kinetic gating" might be important for CcO to avoid deep thermodynamical traps and to maintain both efficient and fast pumping (*23*).

To have a reliable description of substrate/pumped proton transfers in CcO, it is important to carry out careful benchmark calculations to establish the reliability of the simulation protocol and the molecular model for this complex enzyme−membrane system. For building a proper enzyme model for CcO, the issues of particular concern include the treatment of the membrane environment, selection of the titration states of various titratable amino acid residues, and the number of water molecules to include in the hydrophobic region around the active site. A powerful and quantitative benchmark in this regard is the microscopic pK_a calculation of a residue in the active site using thermodynamic integration (TI). The specific residue on which we focus is Glu286 in *Rhodobacter sphaeroides* CcO, which has been experimentally measured (*24*) to have a significantly shifted pK_a of 9.4. Positioned to connect the D-channel and the "hydrophobic cavity" in the active site region, Glu286 is well accepted as the branching point (*25*−*27*) for the substrate versus pumped proton transfers in CcO, though the precise gating mechanism is not clear. Although the pK_a of Glu286 has been reproduced by continuum electrostatics calculations (*28*), the functional importance of this residue and its unique location make it an ideal target for the purpose of quantitatively benchmarking QM/MM protocols and identifying key factors that make a large contribution to its pK_a value. As discussed in previous studies (*29, 30*), although a QM/MM potential is not required for most simple titratable groups, accurate pK_a predictions within the QM/MM framework rely on many technical details such as the proper treatment of electrostatics, a sufficient amount of conformational sampling, and the use of a reliable QM/MM potential. Therefore, the ability to reproduce the experimental pK_a values of key residues serves as an important quantitative measure for validating the reliability of the enzyme model and the simulation protocols being used. In addition, the results from such calculations will provide valuable guidance to the choice of a proper molecular model for a quantitative analysis of proton transfer mechanisms, which are beyond the capability of continuum electrostatic models and semimacroscopic models, especially concerning the role of structural transitions (*31*).

In this paper, we describe a series of pK_a calculations for Glu286 in CcO using the TI protocol with a QM/MM−GSBP approach (*32, 33*); as an additional benchmark for the protocol, calculations have also been done for two somewhat simpler cases, Asp70 in T4 lysozyme and Asp85 in bacteriorhodopsin (bR). We first briefly summarize the enzyme model in the QM/MM−GSBP framework and the protocol used for pK_a calculations. Following a brief summary of the T4 lysozyme and bR results, we discuss the calculated pK_a value of Glu286 and its sensitivity to various factors such as the number of waters in the hydrophobic cavity and the protonation states of other titratable groups, especially the commonly assumed proton loading site, the propionate group of heme$_{a3}$. Finally, we draw a few conclusions regarding the reliability of the QM/MM−GSBP simulation protocol and mechanistic implications of the pK_a calculations on the proton pumping process.

1. COMPUTATIONAL METHODS AND SETUP

The basic simulation protocol used for pK_a calculations in this work is TI with a SCC-DFTB/MM-GSBP potential. Since this protocol has been presented in detail in several previous publications (*29, 30, 32, 33*), we refer the readers to the original references and include only technical details for the specific systems studied here. Although Glu286 in *R. sphaeroides* CcO is the subject of main interest, two other cases have also been examined as additional benchmarks for the pK_a of carboxylic acids in biomolecules; these are Asp70 in T4 lysozyme and Asp85 in bacteriorhodopsin (bR). Asp70 in T4 lysozyme was chosen because it has a large pK_a shift and the system is not complicated by the presence of a membrane, while Asp85 in bR was chosen since the system is simpler than CcO and the pK_a values of critical groups have been better characterized by previous experimental and theoretical studies.

1.1. CcO Simulation Setup. 1.1.1. Enzyme Model. The enzyme model is constructed on the basis of the X-ray structure for the *R. sphaeroides* CcO in the fully oxidized state (PDB entry 1M56) at 2.3 Å resolution (*7*). As noted in previous studies (*11, 34, 35*), two critical issues related to the overall setup concern the number of explicit water molecules included in the interior, especially the hydrophobic cavity near the binuclear site (BNC), and the protonation states of the titratable amino acid residues.

With regard to the issue of water in the protein interior, the protein is first solvated by the standard overlay protocol using a box of equilibrated TIP3P waters, taking care not to add waters in the expected membrane regions. Successive overlays of the water boxes are performed with all solvent molecules within 2.8 Å of any non-hydrogen protein atom removed in each iteration. In addition, the hydrophobic cavity in the active site region is specifically solvated using grand canonical Monte Carlo (GCMC) (*36*) simulations. Following the protocol of Roux et al. (*36*), all water molecules within 15 Å of Glu286 are subjected to Monte Carlo equilibration while all other protein atoms are kept fixed. Of the 34 water molecules in the 15 Å region around Glu286, GCMC simulations predict only 26 water molecules to be stable with six waters in the hydrophobic cavity above Glu286; 14 of these have been resolved in the X-ray structure, and the rest are added to the region above the heme groups near the proposed exit region (four), at the mouth of the D-channel (one), and near the backbone of Trp172 (one). During the subsequent MD simulations, however, one water molecule moves out of the cavity into the D-channel (see Figure 3a,b).

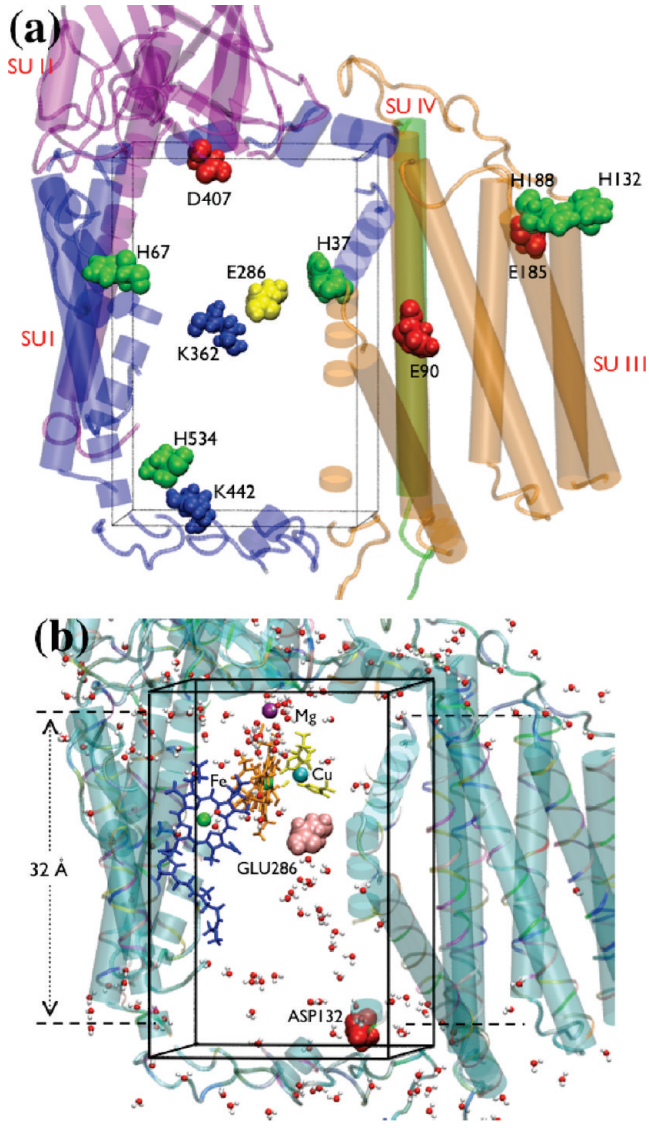

FIGURE 1: Illustration of the computational setup for the CcO system from *R. sphaeroides*. (a) Location of titratable residues predicted to have a significantly shifted pK_a values by MCCE calculations (*11*) (also see Table 2). (b) Partitioning of the system into the inner rectangular region (40 Å × 40 Å × 56 Å) in the GSBP framework; the location of several key residues is indicated, and the thickness of the membrane ($\varepsilon = 2$) is taken to be 32 Å. The water molecules shown are those determined from the X-ray structure (*7*) in the relevant region.

The five remaining waters in the hydrophobic cavity are stable and inhabit the cavity at all times during nanosecond simulations. The predicted number of waters is consistent with the results of Stuchebrukov et al. (*35*) on the thermodynamic properties of internal water in the hydrophobic cavity of CcO where five to six water molecules were found to reside in the cavity. Recent molecular dynamics simulations by Wikstrom et al. (*16, 37*) also suggest that at least four water molecules need to be present in the hydrophobic cavity to facilitate Glu286 side chain rotation and allow proton transfer to occur; an upper limit for the number of waters, however, has not been provided.

An important technical issue related to GCMC simulations is the choice of the excess chemical potential value for water (μ_{ex}). Following the work of Roux et al. on the KcsA channel (*36*), we chose a value for μ_{ex} of −5.8 kcal/mol, though a range of μ_{ex} values from −6.5 to −5.4 kcal/mol have been

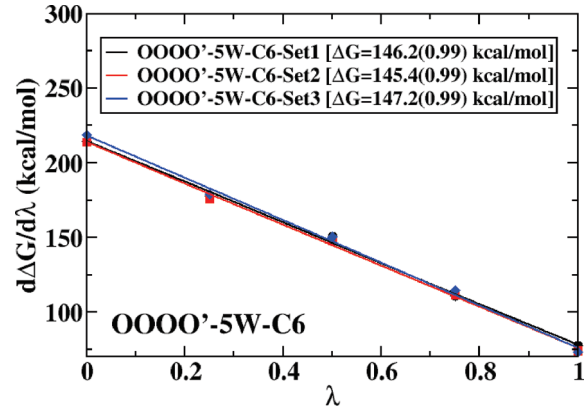

FIGURE 2: Linear λ dependence for $\partial \Delta G^{(1)}_{E^-RCOO(H/D)}/\partial\lambda$ for three independent sets of simulations with the OOOO′−5w−C6 setup.

reported for the TIP3P water model (*38*). The most appropriate value of μ_{ex} to use in conjunction with a specific protein force field is not clear. To assess the sensitivity of the number of predicted waters to μ_{ex}, we have repeated GCMC simulations with a series of μ_{ex} values. As shown in Table 1, as μ changes from −3.0 to −7.0 kcal/mol, the predicted number of waters in the hydrophobic cavity varies from seven to five, which is a fairly narrow range; changing the protonation state of Glu286 does not lead to the change in the predicted number of waters. In most subsequent pK_a simulations, five water molecules are placed in the hydrophobic cavity following the GCMC simulation with a μ_{ex} of −5.8 kcal/mol.

With regard to the protonation states of the titratable groups, recent multiconformation continuum electrostatics (MCCE) (*11*) calculations on CcO suggested that a cluster of residues near the proton uptake (His127−Glu539) and release regions (His93−Glu182) as well as some other residues (Table 2, as shown in Figure 1a) have significantly shifted pK_a values and therefore have nonstandard protonation states depending on the oxidation state of the metal centers. It should be noted that although most of these residues are relatively far from Glu286 or the BNC, a change in their protonation states might have a non-negligible cumulative effect on the energetics at these sites depending on how effectively the protein and membrane environment screen the effect of the charges. We test two sets of protonation states in the pK_a calculations, the MCCE-predicted protonation states for residues in the fully oxidized enzyme (net charge of −6, termed the "C6" set of simulations) and the default titration state of all titratable groups at pH 7 (net charge of −14, term the "C14" set). We note that the current setup does not allow fractional protonation of titratable sites, although the net charge in the C6 set of simulations is rather close to the MCCE prediction (−4.3) at pH 7 for the fully oxidized enzyme (*11*).

The metal centers in all of our calculations are taken to be oxidized to be consistent with the experimental pK_a measurement for the P_R state (*24*). However, the ligation states of the metal centers are not clear from experiments and chosen on the basis of earlier Poisson−Boltzmann (PB) calculations (*39*−*41*). We specifically vary the protonation state of two ligands of Cu_B: water versus hydroxide and neutral versus deprotonated His334. The protonation state of Tyr288, which is cross-linked to Cu_B-bound His284, is also not clear; some researchers believe it is deprotonated

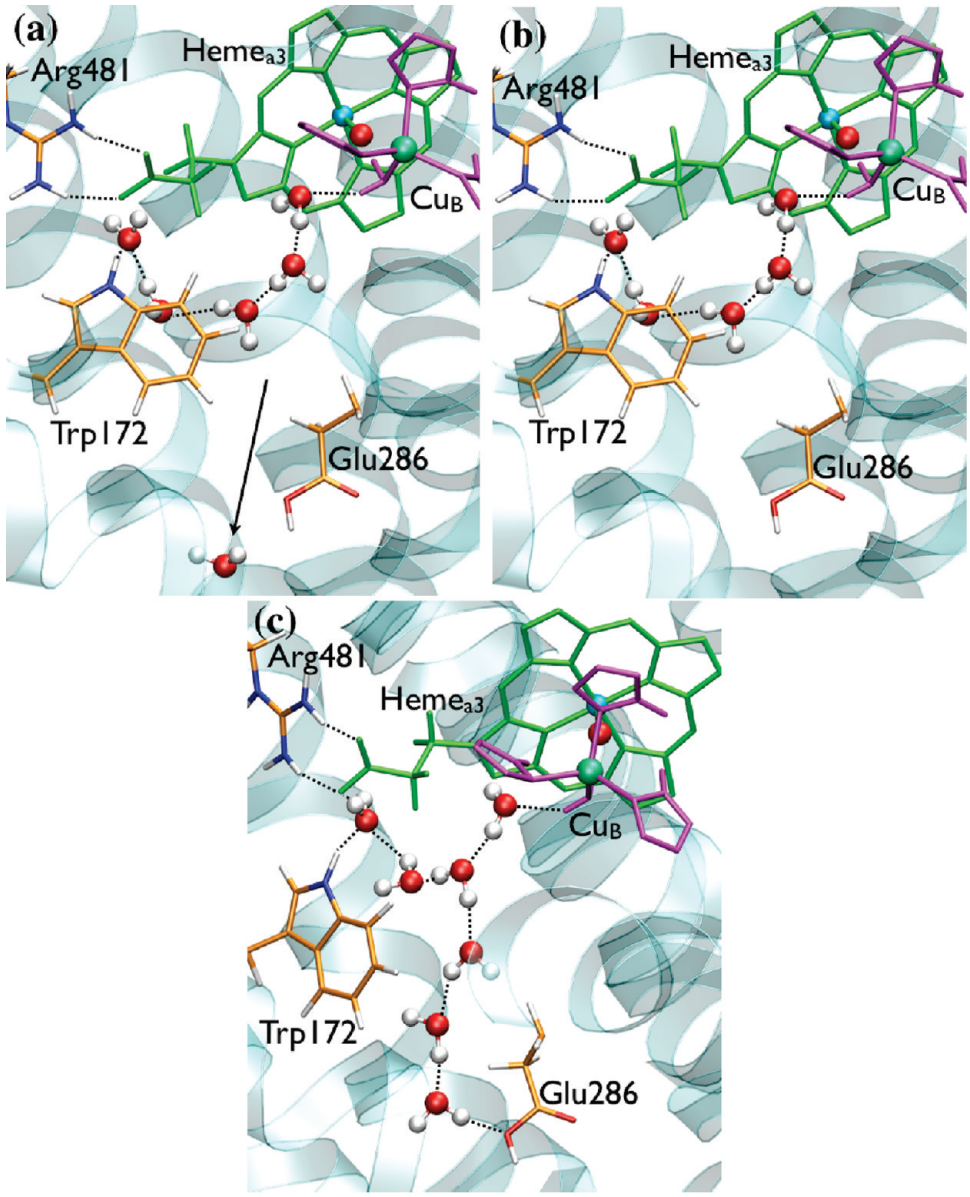

FIGURE 3: Distribution of water molecules in the hydrophobic cavity near the Cu_B center when the simulation is initiated with (a) six, (b) five, or (c) seven water molecules (also see Table 1 for results of GCMC simulations). Note that in panel a one water escapes from the hydrophobic cavity into the D-channel during the simulation, while only in panel c are continuous hydrogen-bonded water wires between Glu286 and both the chemical and physical sites formed simultaneously. Glu286 is protonated in all cases.

Table 1: Number of Waters Added to the Hydrophobic Cavity of CcO in GCMC Calculations as a Function of Excess Chemical Potential (μ_{ex}) for the Water[a]

case	oxidation state	Glu286 protonation state	μ_{ex} (kcal/mol)	no. of waters in the hydrophobic cavity
1	OOOO′	P	−3.0	7
2	OOOO′	P	−4.8	7
3	OOOO′	P	−5.3	7
4	OOOO′	P	−5.8	5
5	OOOO′	dP	−5.8	5
6	OOOO	P	−5.8	5
7	OOOO′	P	−6.3	5
8	OOOO′	P	−7.0	5

[a] The original X-ray structure for *R. sphaeroides* CcO in the fully oxidized state [PDB entry 1M56 (*7*)] with Glu286 in the down orientation is used; the protonation state of titratable residues is the C6 set (see Table 2).

and negatively charged in P_R (*31, 42, 43*), while recent continuum electrostatics calculations predict it to have a high pK_a and therefore be in the neutral form at all oxidation states

Table 2: Amino Acids with Nonstandard Protonation States and Their Positions Relative to Glu286

case	oxidation state	total charge on the enzyme	amino acids altered from default state (subunit)	percentage ionization[a]	distance (Å) to Glu286[b]
C14	OOOO′	−14	Glu286(A)	−	−
			Lys362(A)	−	20
C6	OOOO′	−6	Glu286(I)	−	−
			Lys362(I)	−	20
			Lys442(I)	−	29
			Glu185(III)	−	37
			Glu90(III)	−	21
			Asp407(I)	−	19
			Asp251(III)	−	33
			His67(I)	62	34
			His534(I)	62	37
			His188(III)	63	45
			His37(III)	88	25
			His132(III)	57	30

[a] Predicted by MCCE calculations published in ref *11*. [b] Estimated on the basis of the shortest distance to C_γ of Glu286 in the X-ray structure.

of the enzyme at equilibrium (*11*), which is adopted in the set of calculations presented here. The notation for specifying the metal redox/ligation states is as follows: all four metal centers in the oxidized state with water bound to Cu_B which is termed the OOOO′ state (Cu_A^{2+}, $Fe_{Heme_a}^{3+}$, $Fe^{4+}{=}O_{Heme_{a3}}^{2-}$, $Cu_B^{2+}{-}HOH$) and the oxidized state with hydroxide bound to Cu_B is the OOOO state (Cu_A^{2+}, $Fe_{Heme_a}^{3+}$, $Fe^{4+}{=}O_{Heme_{a3}}^{2-}$, $Cu_B^{2+}{-}OH$). His334 is taken to be charge neutral unless explicitly stated (see Table 4).

1.1.2. GSBP Setup. Since the membrane dynamics is not expected to have a dominant impact on the proton pumping process in *R. sphaeroides* CcO, the GSBP (*44*) protocol has been selected for its computational efficiency; it is also straightforward to include transmembrane potential in the GSBP protocol within the continuum electrostatics framework, although this has not been done in this work. As described in detail previously (*30, 45*), the system is partitioned into inner and outer regions and only the microscopic dynamics of the inner region are followed explicitly; the contributions from the outer region, including bulk solvation effects, are approximated at the Poisson−Boltzmann level. As shown schematically in Figure 1b, we use the rectangular boundary condition for the GSBP setup with dimensions of 40 Å × 40 Å × 56 Å. The outer region has 10562 atoms that are held fixed, while 8447 (7923 protein and 524 waters) atoms that belong to the inner region are allowed to undergo explicit thermal fluctuations. Protein atoms at the boundary of inner and outer regions are constrained according to the previously described protocol (*44*). All bonds involving hydrogen are constrained with SHAKE (*46*) to allow a 2 fs time step. Temperature control is achieved by coupling the system to a Nose-Hoover thermostat (*47*). The entire system is heated to 300 K and equilibrated for ∼200 ps prior to any free energy simulations. We note that all subunits of the CcO monomer have been included in this study, while most previous studies have included either only subunit I or only subunits I and II.

In the PB calculations for the various GSBP components, the static field due to outer region charge distribution, ϕ_S^o, and the reaction field matrix, **M**, a coarse cubic grid of 1.6 Å spacing, and a fine grid of 0.4 Å spacing are used in focusing calculations. To evaluate the contribution of the inner region charge distribution to the total electrostatic solvation free energy, the charge density of the inner region is expressed as a basis set expansion using Legendre polynomials up to order 12 (*48*). The membrane−solvent environment is treated implicitly with a dielectric model, and the protein−solvent boundary is determined using the atomic radii of Nina et al. (*49*). The membrane thickness is set to 32 Å with the dielectric constant for the membrane and the bulk solvent set to 2.0 and 80.0, respectively. A dielectric constant of 1.0 is assigned to the protein in the inner region and 4.0 in the outer region. To be consistent with the GSBP protocol, the extended electrostatics model (*50*) is used to treat the electrostatic interactions among inner region atoms in which interactions beyond 12 Å are treated with multipolar expansions, including the dipolar and quadrupolar terms.

1.1.3. QM/MM Setup and ab Initio Parametrization of Metal Centers. In all calculations reported here, only the side chain of the titratable residue (Glu286 in CcO) is treated with a QM approach (see section 1.3) while the rest of the system is treated using the all-atom CHARMM22 force field (*51*). As discussed in earlier publications (*30, 52*), one of the key issues in QM/MM simulations that involve a significant change in the QM charge distribution is the treatment of the QM/MM frontier. In our set of calculations, we follow the EXGR scheme with the link atom added between C_β and C_γ of the Glu286 side chain. The EXGR scheme involves zeroing out the partial charges on the entire MM host group and has been shown to avoid spurious QM/MM electrostatic interactions; it has been shown to give satisfactory proton affinity values in gas phase models (*52*) and pK_a values for protein and solution systems (*53*).

As for the MM part, force field parameters for $heme_{a3}$, $heme_a$, and Cu_B motifs are not available in CHARMM22 (*51*) and hence have to be developed. For this purpose, a simple gas phase model is constructed for the Cu_B metal center, in which a Cu(II) ion is coordinated with three methyl imidazoles and a hydroxide or water molecule; Tyr288, which is cross-linked to His284, is modeled as a methyl group bound to N_ε of His284. The choice of oxidation state and ligands for the Cu_B center in the gas phase models is appropriate for the states (OOOO and OOOO′) used in the pK_a calculations. The gas phase model for $heme_{a3}$ is constructed with the farnesyl chains in the porphyrin ring substituted with hydrogens, and the axial histidine (His419) ligand coordinated to the iron is replaced with a methyl imidazole while the other axial ligand is oxygen [Fe(IV)═O]. For the Fe(IV)═O state of $heme_{a3}$, the triplet electronic state is calculated since it is the lowest in energy among the singlet, triplet, and quintuplet electronic states. The gas phase model for $heme_a$ is similar to that for $heme_{a3}$ except that both the axial histidine ligands (His421 and His102) are replaced with methyl imidazoles. The doublet state is found to be most stable for the Fe(III) state of $heme_a$ among doublet, quartet, and sextuplet electronic states. Geometry optimizations of the gas phase models are done at the B3LYP level (*54, 55*) using the Hay−Wadt pseudopotential/basis (Lanl2dz) (*56*−*58*) for Cu/Fe and 6-31G* for other atoms (*59*). All calculations are done with Gaussian03 (*60*).

Using these optimized gas phase models, partial charges are assigned on the basis of ESP charges (*61, 62*) calculated at the 6-311+G** level (*63*). The van der Waals parameters are then fitted using the standard protocol for the CHARMM force field (*51*): a water molecule is placed at a series of distances and orientations relative to the gas phase model, and the van der Waals parameters are then fitted such that the QM interaction energies are reproduced with the water described by the TIP3P model (parameters included in the Supporting Information).

1.2. Model Benchmark Systems: T4 Lysozyme and Bacteriorhodopsin (bR). 1.2.1. Simulation Setup. As the starting atomic configuration, the X-ray structure for lysozyme from T4 bacteriophage at 1.9 Å resolution (PDB entry 1L54) (*64*) is used and all amino acids are kept in their standard titration states. For bR, the X-ray structure for the ground state at 1.5 Å resolution (PDB entry 1C3W) (*65*) is used; all amino acids are kept in their physiological protonation state except Asp96 and Asp115, which are known to be protonated in the ground state (*66*). The *all-trans*-retinal is treated using the CHARMM force field developed in refs *67* and *68*. the Schiff base is kept protonated throughout the simulations, consistent with the previous prediction for the ground-state bR using continuum electrostatics (*69*). For both structures,

successive overlays of a 25 Å water sphere are performed to solvate the protein, removing after each iteration all solvent molecules that are within 2.8 Å of any non-hydrogen protein atom. The added solvent molecules are relaxed at 300 K for 20 ps with all protein and crystallographic water molecules held fixed. The solvation layers beyond 18 Å are deleted, providing the final structure used as the starting point for subsequent simulations. In the TI simulations, the inner region was further partitioned into Newtonian and Langevin regions. Atoms beyond 20 Å are fixed; those between 16 and 20 Å are treated with Langevin dymanics, while the rest are treated with standard Newtonian dynamics. The protein atoms in the Langevin region are harmonically constrained with force constants determined from the crystallographic *B*-factors. All bonds involving hydrogen are constrained with SHAKE (*46*) to allow a 2 fs time step. The entire system is heated to 300 K and equilibrated for 200 ps prior to any free energy simulations.

1.2.2. GSBP Setup. In the GSBP calculations, the protein is partitioned into a 20 Å spherical inner region with the remaining portion of the system in the outer region. The static field due to outer region atoms, ϕ_s^o, and the reaction field matrix, **M**, are evaluated using PB calculations with a focusing scheme that places a 56 Å cube of fine grid (0.4 Å) into a larger 132 Å cube of coarse grid (1.2 Å). The inner region charge density is expressed using the first 20th-order spherical harmonics with a total of 400 basis functions. Other details of the PB calculations (dielectric constants for different regions and atomic radii) are the same as in the CcO setup.

1.3. pK_a Calculations. The pK_a calculations are carried out using the TI approach (*70, 71*) within the dual-topology single-coordinate (DTSC) scheme (*29, 30, 32*). In this approach, the dominant contribution to the total free energy of deprotonation is from the electrostatic free energy change [$\Delta G^{(1)}_{E-RCOO(H/D)}$] associated with converting the acidic proton to a dummy atom (D), i.e., the transformation from E−RCOOH to E−RCOOD, where E represents the protein and R-COOH is the titratable acidic residue (Glu286 in CcO, Asp85 in bR, and Asp70 in T4 lysozyme). The corresponding free energy derivative is given by

$$\frac{\partial \Delta G^{(1)}_{E-RCOO(H/D)}}{\partial \lambda} = \langle U_{elec}^{E-RCOOD}[X_{E-RCOO(H/D)}] - U_{elec}^{E-RCOOH}[X_{E-RCOO(H/D)}]\rangle_\lambda \quad (1)$$

which represents the QM/MM energy difference averaged for a specific coupling parameter λ using the same set of coordinates [$X_{E-RCOO(H/D)}$] for both protonation states, E−RCOO(H/D). The total electrostatic free energy contribution [$\Delta G^{(1)}_{E-RCOO(H/D)}$] is determined by integrating the converged free energy derivatives [$\partial \Delta G^{(1)}_{E-RCOO(H/D)}/\partial\lambda$] over λ from 0 to 1.

Even though the absolute pK_a of a residue can, in principle, be estimated using the protocol described above, to do so the solvation free energy of a proton has to be taken into account. When considering "pK_a shifts" relative to a reference molecule in solution the proton solvation term, which is difficult to measure or compute accurately, does not contribute. Therefore, as in recent studies (*53*), we choose to compute the pK_a shift relative to acetic acid in solution [experimental pK_a ∼ 4.8 (*72*)], which also helps to cancel other contributions, such as the zero-point energy difference between the protonated and deprotonated states and van der Waals interactions involving the acidic proton (*29*). The lack of explicit treatment of electronic polarization in the protein and solvent is also expected to partially cancel out in such pK_a shift calculations, although the degree of cancellation remains an interesting topic that will be discussed in separate work (J. Yu and Q. Cui, work in progress).

Finally, as also noted in the recent study (*53*), since $\Delta G^{(1)}_{E-RCOO(H/D)}$ is electrostatic in nature, one expects that the free energy derivative depends linearly on the coupling parameter λ (*73*). Rigorously speaking, this is only true if there are no major structural transitions in the protein during the titration process, which can cause the distribution of an "energy gap" (rhs of eq 1) to deviate from Gaussian and therefore nonlinearity in the $\partial \Delta G^{(1)}_{E-RCOO(H/D)}/\partial\lambda - \lambda$ relation (*74, 75*). Nevertheless, many previous studies found that the approximate linear relation holds even in the presence of distinct local structural rearrangements (*75, 76*).

1.3.1. Statistical Analysis. During the thermodynamic integration-based pK_a simulations, the net charge of the system changes. The response of the entire protein to the altering charge can be substantial and slow to converge due to its collective nature. Therefore, it is crucial to carefully monitor the statistical and sampling errors and reproducibility of the microscopic pK_a simulations. In this study, multiple independent trajectories have been carried out for the key sets of pK_a simulations (see the tables). For each set of pK_a simulation, the average free energy derivative value of a particular λ is determined using a block averaging scheme that has been discussed in detail in recent studies (*53, 76*). For bR and T4 lysozyme, the statistical analyses are summarized together with the pK_a results in Table 3. For CcO, the amount of simulation identified as the equilibrating phase and the number and size of blocks for the equilibrated data are summarized in Table 6, and the statistical average and error for different λ values in different sets of simulations are summarized in Table 5. The amount of data excluded from meaningful ensemble average calculations ranges as much as ∼1.2 ns, which highlights the importance of careful statistical analysis of the simulation data. The typical statistical error is on the order of 0.4−1.4 kcal/mol.

1.3.2. B3LYP/MM Correction. In the SCC-DFTB/MM method (*77*), the electrostatic interaction between QM and MM atoms is calculated using Mulliken charges on the QM atoms

$$\hat{H}_{elec}^{SCC/MM} = \sum_{I\in MM}\sum_{J\in QM}\frac{q_I \Delta q_J}{r_{IJ}} \quad (2)$$

where Δq_J is the Mulliken charge on QM atom *J*. This formulation is consistent with the way that charge relaxation is achieved for the QM atoms in SCC-DFTB (*78*). Since the QM electron distribution is represented by atom-based point charges, this approximation does not allow MM charges to interact with different orbitals on a QM atom differently. The more rigorous QM/MM coupling treatment includes the contribution from the MM point charges in the one-electron integrals, which is done in B3LYP/MM calculations (*79*). Therefore, correcting SCC-DFTB/MM results based on B3LYP/MM calculations improves not only the QM level itself but also the way that MM region interacts with and polarizes the QM region. The correction is done on the basis

Table 3: Free Energy Derivatives, $\Delta G^{(\lambda)}_{E-RCOO(D/H)}$, p$K_a$, and Statistical Analysis of pK_a Simulations for Asp70 in T4 Lysozyme and Asp85 in Bacteriorhodopsin[a]

λ	Asp70 T4	Asp85 bR (set 1)	Asp85 bR (set 2)	Asp85 bR (set 3)	Asp85 bR (set 4)
0.00	218.2 (0.4)	202.6 (1.1)	190.8 (1.9)	193.6 (1.5)	200.7 (0.6)
0.25	183.4 (0.4)	154.7 (0.5)	160.1 (0.4)	158.7 (0.5)	168.2 (1.4)
0.50	140.7 (0.5)	129.7 (0.8)	131.8 (0.4)	131.6 (1.2)	138.4 (0.9)
0.70	108.6 (0.5)	–	–	–	–
0.75	–	91.7 (0.4)	100.4 (1.2)	94.1 (0.3)	103.2 (1.0)
0.90	73.5 (0.6)	–	–	–	–
1.00	49.5 (0.8)	59.6 (0.9)	56.3 (1.2)	57.9 (1.8)	60.8 (0.9)
$\Delta G^{(\lambda)}_{E-RCOO(D/H)}$[b]	138.0 (0.99)	128.0 (0.99)	128.1 (0.99)	127.2 (0.99)	135.8 (0.99)
pK_a[c]	0.0	2.1 (1.9)	2.2 (1.8)	1.5 (1.4)	7.8 (7.3)

	Asp70 T4		Asp85 bR (set 1)		Asp85 bR (set 2)		Asp85 bR (set 3)		Asp85 bR (set 4)	
λ	prod(equi)	τ (n)	prod(equi)	τ (n)	prod(equi)	τ (n)	prod(equi)	τ (n)	prod(equi)	τ (n)
0.00	3.2 (0.5)	40 (80)	2.0 (0.4)	26 (62)	2.0 (1.1)	12 (25)	2.5 (1.2)	22 (59)	2.5 (1.5)	17 (59)
0.25	3.2 (1.1)	40 (53)	2.0 (0.8)	15 (80)	2.0 (1.0)	14 (42)	2.5 (1.1)	18 (78)	2.5 (0.9)	59 (27)
0.50	3.2 (0.5)	40 (80)	2.0 (0.9)	20 (55)	2.0 (1.0)	12 (50)	2.5 (1.3)	16 (75)	2.5 (1.1)	27 (51)

	Asp70 T4		Asp85 bR (set 1)		Asp85 bR (set 2)		Asp85 bR (set 3)		Asp85 bR (set 4)	
λ	prod(equi)	τ (n)	prod(equi)	τ (n)	prod(equi)	τ (n)	prod(equi)	τ (n)	prod(equi)	τ (n)
0.70	3.2 (0.5)	40 (69)	–	–	–	–	–	–	–	–
0.75	–	–	2.0 (1.1)	23 (39)	2.0 (1.1)	10 (50)	2.5 (0.7)	26 (69)	2.5 (1.1)	22 (63)
0.90	3.2 (0.4)	40 (71)	–	–	–	–	–	–	–	
1.00	3.2 (0.5)	40 (76)	2.0 (1.0)	13 (77)	2.0 (1.1)	16 (38)	2.5 (1.6)	20 (45)	2.5 (0.8)	56 (30)

[a] The free energy derivatives are given in kilocalories per mole, and the values in parentheses are statistical errors. [b] Computed on the basis of the linear fit of the free energy derivatives vs λ and subsequent integration over λ; the values in parentheses are the R^2 values for the linear fit. [c] The pK_a is computed using the calculated pK_a shift relative to the acetic acid in solution, whose experimental value is 4.8 (*72*); the numbers in parentheses include correction using single-point B3LYP/6-311+G**/MM energy calculations at 500 SCC-DFTB/MM geometries with a second-order cumulant expansion (see section 1.3.2). [d] prod(equi) gives the total amount of simulation time (in nanoseconds) and the segment identified as equilibration (in parentheses). τ gives the size of the block (in picoseconds), and n gives the total number of blocks in the final free energy derivative calculations.

Table 4: Summary of Computed pK_a Values for Glu286 in the P_R State of CcO Using a SCC-DFTB/MM-GSBP-Based Thermodynamic Integration Approach[a]

setup	ligation state of Cu_B	no. of waters in the hydrophobic cavity	net charge on enzyme	His334/PRD_{a3} protonation state	computed pK_a	perturbation[b]
OOOO′−5w−C6−set 1	H_2O	5	−6	0/−1	15.4 (11.3)	− (−)
OOOO′−5w−C6−set 2	H_2O	5	−6	0/−1	14.8 (11.7)	−1.3 (1.1)
OOOO′−5w−C6−set 3	H_2O	5	−6	0/−1	16.1 (12.1)	−0.7 (−0.3)
OOOO′−7w−C6	H_2O	7	−6	0/−1	11.8 (11.8)	−3.6 (1.1)
OOOO−5w−C7−set 1	OH^-	5	−7	0/−1	18.8 (15.8)	3.4 (4.5)
OOOO−5w−C7−set 2	OH^-	5	−7	0/−1	19.8 (16.2)	4.4 (4.9)
OOOO−5w−C7−set 3	OH^-	5	−7	0/−1	19.6 (16.0)	4.2 (4.7)
OOOO−5w−C6−PRD_{a3}	OH^-	5	−6	0/0	11.0 (8.1)	−3.4 (−3.2)
OOOO′−5w−C7−H334	H_2O	5	−7	−1/−1	19.8 (17.6)	4.4 (6.3)
OOOO′−5w−C14	H_2O	5	−14	0/−1	22.8 (21.3)	8.1 (9.8)

[a] The experimental measured value is 9.4 (*24*); the numbers in parentheses include correction using single-point B3LYP/6-311+G**/MM energy calculations at 500 SCC-DFTB/MM geometries with a second-order cumulant expansion (see section 1.3.2). [b] Using the first set of OOOO′−5w−C6 results as a reference.

of a straightforward one-step free energy perturbation calculation

$$\Delta G_{\text{B3LYP-SCC}} = -kT \ln\langle e^{-\beta(U_{\text{B3LYP/MM}} - U_{\text{SCC/MM}})}\rangle_{\text{SCC/MM}} \quad (3)$$

at both end states ($\lambda = 0.0$ or 1.0). The difference between the perturbative correction at the two end states gives the B3LYP/MM correction to the free energy of deprotonation [$\Delta G^{(\lambda)}_{E-RCOO(H/D)}$]. Since only a small number (500) of snapshots from SCC-DFTB/MM trajectories are used, a second-order cumulant expansion is used to improve the numerical stability of the perturbation calculation

$$\Delta G_{\text{B3LYP-SCC}} = \langle U_{\text{B3LYP/MM}} - U_{\text{SCC/MM}}\rangle_{\text{SCC/MM}} - \frac{\beta}{2}[\langle (U_{\text{B3LYP/MM}} - U_{\text{SCC/MM}})^2\rangle_{\text{SCC/MM}} - \langle U_{\text{B3LYP/MM}} - U_{\text{SCC/MM}}\rangle^2] \quad (4)$$

As discussed extensively in the literature (*80*), such one-step perturbation is effective only if the configuration space at the two levels overlaps significantly; this is assumed to be the case considering the previous observation (*81, 82*) that SCC-DFTB often gives reliable geometries and energetics compared to B3LYP.

2. RESULTS AND DISCUSSION

In this section, we first briefly discuss results for the somewhat simpler benchmark systems, T4 lysozyme and bacteriorhodopsin. Next, we present the results for CcO and discuss in detail the various factors that may influence the computed pK_a for Glu286.

2.1. Benchmark Systems: T4 Lysozyme and Bacteriorhodopsin. 2.1.1. pK_a of Asp70 in T4 Lysozyme. As discussed in section 1, Asp70 in T4 lysozyme is selected because it

Table 5: Free Energy Derivatives and $\Delta G^{(1)}_{E-RCOO(D/H)}$ from pK_a Simulations of Glu286 in CcO with Different Setups[a]

λ	OOOO′−5w−C6−set 1	OOOO′−5w−C6−set 2	OOOO′−5w−C6−set 3
0.00	214.6 (1.2)	214.1 (1.4)	218.8 (1.4)
0.25	178.2 (1.1)	176.2 (0.8)	178.9 (1.6)
0.50	150.8 (0.9)	148.2 (0.7)	150.4 (0.7)
0.75	110.6 (0.9)	111.8 (1.1)	114.5 (0.7)
1.00	77.6 (0.5)	74.6 (0.6)	73.3 (0.9)
$\Delta G^{(1)}_{E-RCOO(D/H)}$	146.2 (0.98)	145.4 (0.99)	147.2 (0.99)
λ	OOOO−5w−C7−set 1	OOOO−5w−C7−set 2	OOOO−5w−C7−set 3
0.00	218.9 (1.3)	224.3 (1.6)	218.6 (0.6)
0.25	176.8 (1.0)	180.9 (1.2)	177.3 (0.3)
0.50	151.8 (0.8)	155.7 (0.7)	155.3 (0.8)
0.75	129.1 (0.4)	127.1 (0.6)	125.3 (2.7)
1.00	76.8 (0.7)	77.2 (0.8)	80.2 (0.5)
$\Delta G^{(1)}_{E-RCOO(D/H)}$	151.0 (0.98)	152.3 (0.98)	152.0 (0.98)
λ	OOOO′−7w−C6	OOOO−5w−C6−PRD$_{a3}$	OOOO′−5w−C7−H334
0.00	208.0 (0.6)	196.7 (1.0)	215.3 (0.8)
0.25	180.1 (1.0)	167.3 (0.5)	182.0 (1.0)
0.50	140.7 (0.9)	142.8 (0.4)	155.8 (0.4)
0.75	112.1 (0.5)	114.7 (1.3)	125.3 (1.0)
1.00	68.9 (0.8)	79.0 (0.9)	80.9 (1.0)
$\Delta G^{(1)}_{E-RCOO(D/H)}$	141.9 (0.99)	140.2 (0.99)	151.9 (0.99)

[a] See the footnote of Table 3 for the format and notation used.

has a large pK_a shift due to its involvement in salt bridge interaction with His31 (*83*); in addition, the system is not membrane-bound, and therefore, the computed pK_a reflects the intrinsic accuracy of the TI protocol with the SCC-DFTB/MM-GSBP potential for carboxylic acid in proteins, without complication from the simplified treatment of the membrane environment.

The H31−D70 cluster in T4 lysozyme is solvent accessible from one side and close to a hydrophobic core on the other side. Because of their proximity and salt bridge interaction, the titration states of His31 and Asp70 are expected to be coupled. The experimentally measured pK_a of His31 is shifted up to 9.1, while the pK_a of Asp70 is shifted down to 0.5. In the current pK_a calculation for Asp70, the His31 is in the protonated state, which is justified by the large difference between the intrinsic pK_a values of the two residues (*84*). During simulations, the H31−D70 salt bridge remains intact and flipping of His31 into solution has not been observed even for the $\lambda = 0$ window (protonated Asp70), though large fluctuations in the salt bridge distance are seen. The protein structure remains stable during the pK_a simulations with a rmsd of 0.5 Å for the backbone C_α atoms (inner region atoms only). The calculated pK_a shift is −4.0 pK_a units, which is in good agreement with the experimentally measured value of −3.5 (*85*), indicating that the current computational protocol gives reasonably accurate pK_a shifts for carboxylic acids such as Asp and Glu in proteins.

2.1.2. pK_a of Asp85 in Bacteriorhodopsin (bR). In CcO, the interplay between the membrane hydrophobicity and complex electrostatics modulated by polar amino acids and trapped water molecules controls the pK_a of Glu286, and all these factors need to be taken into consideration for a quantitative prediction of pK_a. To understand whether the complex membrane electrostatics can be reliably captured within the SCCDFTB/MM-GSBP protocol, we compute the pK_a of Asp85 in the ground-state bR. The choice of bR as a benchmark is motivated by the fact that the system is experimentally (*66, 86, 87*) and theoretically (*69, 88, 89*) much better characterized than CcO, and the pK_a values of groups such as Asp85 are unambiguously known (*66*), unlike the case of Glu286 in CcO, whose pK_a is an apparent kinetic value determined using a simple reaction scheme (see below) (*24*).

Four sets of pK_a calculations have been conducted for Asp85 in bR. Sets 1 and 2 simply use independent seeds for sampling; set 3 differs in the dielectric constant used for the protein in the outer GSBP region ($\varepsilon_P = 4$ vs $\varepsilon_P = 1$ in the other three sets), while in set 4, the proton release group (PRG, cluster of Glu194/Glu204 near the extracellular surface) is treated as deprotonated. We note that the precise identity of the PRG is still under debate; on the basis of our recent study on this issue (*89*), this study adopts the simplified model where the protonated PRG (sets 1−3) includes Glu194/204 with Glu194 in the protonated state, while the deprotonated PRG (set 4) includes deprotonated Glu194/204. The sampling time for each λ window is typically 2.5 ns following careful statistical analysis. The calculated pK_a values are 2.2, 2.1, 1.5, and 7.8, respectively. The first three values are in good agreement with the experimental value of 2.6 (*66*). The last value of 7.8 is significantly higher, which is in fact consistent with the experimental observation that the pK_a of Asp85 is significantly shifted up to ∼7.5 when the proton release group is deprotonated or when Arg82 near that region is mutated into a neutral residue (Ala/Gln) (*66*); we note, however, the comparison to the WT experiment with the deprotonated PRG is not straightforward because the experimental value is for the M kinetic state, which has a number of essential structural differences compared to the ground-state bR. Performing the B3LYP/6-311+G**/MM single-point correction (eq 4) leads to a very small difference between bR and the solution reference of ∼1.0 kcal/mol. Therefore, these calculations clearly show that the SCC-DFTB/MM-GSBP scheme describes the electrostatics and pK_a shifts in membrane proteins like bR in a reproducible and satisfactory manner.

2.2. pK_a of Glu286 in CcO. The pK_a of Glu286 has been estimated from kinetic experiments to be 9.4 (*24*), but FTIR

data (*90, 91*) showed no deprotonation of Glu286 even at pH >11. Continuum electrostatics calculations by Stuchebrukhov et al. on CcO models resembling our OOOO and OOOO′ states predicted pK_a values in the range of 9.4−24.1 (Table 3 of ref *28*), depending on the dielectric constant used for the interior cavities (80/20/15/4); the protein was assigned a dielectric constant of 4 throughout their study. MCCE pK_a calculations by Gunner et al. (*11*) predicted a pK_a of >10 for Glu286 in the OOOO′ state. Although continuum electrostatic calculations have been able to reproduce the pK_a of Glu286, the pK_a value is sensitive to the value of dielectric "constants" for the heterogeneous protein component and water-filled cavities. In the following, we discuss in detail results of microscopic pK_a calculations for Glu286. As emphasized above, the goal of these calculations is to understand the sensitivity of Glu286 pK_a to various environmental factors such as the number of waters in the hydrophobic cavity and the protonation state of various titratable groups, including ligands of the Cu_B center (water and His334) and the assumed pumped proton loading site.

2.2.1. Statistical Analysis and Convergence Behavior of $\partial\Delta G^{(l)}_{E-RCOO(H/D)}/\partial\lambda$. First, we discuss the issue of convergence of the microscopic TI simulations using the OOOO′ state with five waters in the hydrophobic cavity as a specific example; the MCCE protonation states for the titratable residues (see Table 2 and section 2.2.2 below) are used. Three independent sets of simulations have been carried out, all starting with the GCMC (using the excess chemical potential $\mu_{ex} = -5.8$ kcal/mol) equilibrated structure with five waters in the hydrophobic cavity but different initial velocities. Free energy derivatives are calculated for five λ values (0.0, 0.25, 0.5, 0.75, and 1.0) with ∼2.0−4.0 ns of sampling in each window (see Table 6). The final value of $\partial\Delta G^{(l)}_{E-RCOO(H/D)}/\partial\lambda$ corresponding to each λ is determined in the forward direction using statistical analysis discussed in section 1.3.1. Figure 2 shows the plot of $\partial\Delta G^{(l)}_{E-RCOO(H/D)}/\partial\lambda$ versus λ for the three different sets, which show that the linear approximation once again works well. As shown in Table 5, the $\partial\Delta G^{(l)}_{E-RCOO(H/D)}/\partial\lambda$ values in some λ windows differ by ∼1−5 kcal/mol among the three sets of simulations, which is substantially larger than the statistical uncertainty of the free energy derivative, reflecting the different phase space explored in the independent sets of simulation. Nevertheless, integration of the linear equations obtained from the linear fit of $\partial\Delta G^{(l)}_{E-RCOO(H/D)}/\partial\lambda$ values gives a fairly narrow range for $\Delta G^{(l)}_{E-RCOO(H/D)}$ between 146.4 and 147.7 kcal/mol, which corresponds to a pK_a for Glu286 in the range of 15.2−16.5. With the B3LYP/6-311+G(d,p)/MM single-point correction included, which was found to improve the description of QM/MM interactions in our previous pK_a studies (*29*), our best pK_a estimate with the OOOO′−5w−C6 model falls in a narrow range of ∼11.0−11.8 (Table 4). As discussed below (section 2.2.6), these estimates are not too different from experimental values of ∼9.4, although we should consider the kinetic nature (*24*) of the experimental value.

2.2.2. Effect of the Protonation State of Titratable Amino Acid Residues on the pK_a of Glu286. As discussed in section 1.1.1, one of the issues of major concern in CcO is the protonation state of titratable groups in the protein. If we use the default titration states for all titratable groups, including those found to have significantly perturbed pK_a values by MCCE calculations (shown in Figure 1a and Table 2), the total charge on the enzyme increases to −14 from the net charge of −6 as in most pK_a calculations in this work, where the MCCE predicted protonation states are used. As shown in Table 4, the predicted pK_a for Glu286 in the −14 charge state (OOOO′−5w−C14) is significantly higher by ∼8 pK_a units than that predicted for the OOOO′−5w−C6 setup. Since most perturbed residues are relatively far from Glu286, this observation indicates that unlike soluble proteins where a large number of water dipoles effectively screen out charges, the low-dielectric membrane and the lack of a large number water molecules in CcO lead to less effective screening of the electrostatics. In this regard, we note that almost all previous microscopic simulations (*14*−*16, 26, 92, 93*) reported for CcO have not explicitly addressed the issue of protonation states of titratable groups, which is worrisome.

2.2.3. Effect of Waters in the Hydrophobic Cavity. The number of waters in the hydrophobic cavity around Glu286 in CcO has been a subject of much discussion (*34, 35*). The fact that no water molecules are observed in the hydrophobic cavity in any of the published X-ray structures suggests that water molecules in this region are highly mobile and the cavity becomes transiently filled with water molecules during the catalytic cycle to help mediate proton transfer. From a functional prespective, the presence of waters in the active site region is imperative since the catalytic cycle of CcO involves proton transfer over long distances (∼10−15 Å) and water is continuously produced during the catalytic cycle.

To probe the sensitivity of the pK_a of Glu286 to the number of waters in the hydrophobic region, we carry out pK_a calculations for the OOOO′ state with two setups that differ in the number of water molecules in the hydrophobic cavity. As discussed in section 2.2.1, with the GCMC-equilibrated five-water structure (Figure 3b), our calculations reproducibly give (see Table 4) a pK_a of 14.8−16.4 (without B3LYP/MM correction). The five waters inhabit the hydrophobic cavity at all times during the nanosecond scale trajectories, but steady water wires connecting Glu286 to either the substrate (Cu_B) or the postulated pumped proton loading (PRD_{a3} of $heme_{a3}$) site are not observed. Therefore, another set of simulations is carried out in which two extra waters are added to the hydrophobic cavity above Glu286. Interestingly, with these extra waters, continuous and stable water wires are frequently formed between Glu286 and both the Cu_B center and PRD_{a3} (Figure 3c). As shown in Table 4, the pK_a of Glu286 decreases significantly from 15.4 to 12.1 upon going from the five- to seven-water case. Comparison of the $\partial\Delta G^{(l)}_{E-RCOO(H/D)}/\partial\lambda$ values for the two sets of simulations (Table 5) indicates that the lower pK_a value in the seven-water case is due to an increased level of stabilization of both the deprotonated and protonated states via better solvation, which is evident from the integrated value of the water radial distribution function averaged over both carboxylic oxygens of Glu286 (Figure 4). When the B3LYP/6-311+G(d,p)/MM single-point corrections are included, however, the computed pK_a (∼11.0−12.0) becomes fairly insensitive to the number of water molecules in the hydrophobic cavity (Table 4). This is largely because the B3LYP correction is more important when the ionized Glu is less solvated, relative to the solution reference; when Glu is well solvated as in the seven-water case, the B3LYP correction largely cancels out between the protein and solution reference, as also found for the bR case (see section

Table 6: Statistical Analysis of pK_a Simulations of Glu286 in CcO with Different Setups[a]

	OOOO′−5w−C6−set 1		OOOO′−5w−C6−set 2		OOOO′−5w−C6−set 3	
λ	prod(equi)	τ (n)	prod(equi)	τ (n)	prod(equi)	τ (n)
0.0	4.0 (1.3)	19 (56)	2.5 (1.2)	18 (72)	2.0 (0.5)	25 (60)
0.25	4.0 (1.7)	26 (53)	2.5 (1.5)	27 (37)	2.0 (1.1)	18 (50)
0.5	4.0 (2.0)	14 (90)	2.5 (1.0)	31 (48)	2.0 (0.8)	19 (63)
0.75	4.0 (1.4)	39 (90)	2.5 (0.9)	47 (34)	2.0 (0.7)	24 (54)
1.0	4.0 (1.4)	36 (67)	2.5 (1.3)	39 (31)	2.0 (0.8)	32 (38)

	OOOO−5w−C7−set 1		OOOO−5w−C7−set 2		OOOO−5w−C7−set 3	
λ	prod(equi)	τ (n)	prod(equi)	τ (n)	prod(equi)	τ (n)
0.0	2.0 (1.0)	20 (50)	1.8 (0.7)	24 (46)	1.8 (0.7)	25 (44)
0.25	2.0 (1.0)	32 (30)	1.8 (0.8)	15 (67)	1.8 (0.9)	19 (47)
0.5	2.0 (0.6)	46 (30)	1.8 (0.5)	20 (65)	1.5 (0.6)	17 (53)
0.75	2.0 (0.8)	26 (65)	1.8 (0.7)	18 (61)	1.5 (0.5)	27 (38)
1.0	2.0 (1.0)	20 (48)	1.8 (0.6)	22 (55)	1.8 (0.9)	14 (64)

	OOOO′−7w−C6		OOOO−5w−C6−PRD$_{a3}$		OOOO′−5w−C7−H334		
λ	prod(equi)	τ (n)	prod(equi)	τ (n)	prod(equi)	τ (n)	
0.0	2.0 (0.9)	11 (100)	2.0 (0.8)	16 (75)	1.5 (0.8)	11 (64)	1.5 (0.9)
0.25	2.0 (0.8)	17 (71)	2.0 (0.7)	13 (100)	1.5 (0.8)	18 (39)	1.6 (0.8)
0.5	2.0 (0.9)	18 (61)	2.0 (0.8)	22 (55)	1.5 (0.9)	10 (60)	1.6 (0.4)
0.75	2.0 (1.0)	8 (125)	2.0 (0.9)	28 (40)	1.5 (1.0)	10 (50)	1.6 (0.8)
1.0	2.0 (0.9)	13 (84)	2.0 (1.3)	12 (58)	1.5 (1.0)	16 (31)	1.6 (1.1)

[a] See the footnote of Table 3 for the format and notation used.

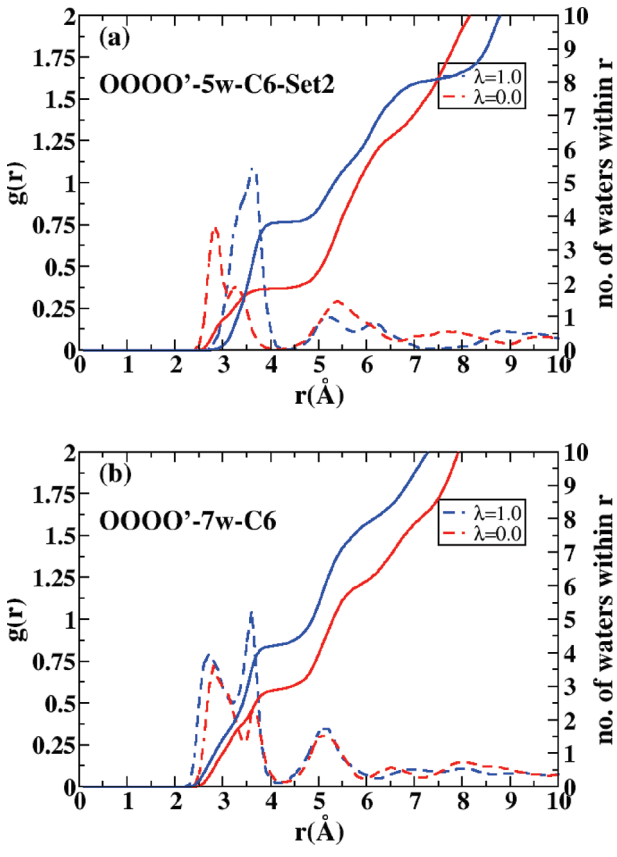

FIGURE 4: Comparison of the water oxygen radial distribution function (RDF, dotted lines) around Glu286 oxygens (averaged over both oxygens) and the integrated RDF (solid lines) from the λ = 0.0 and 1.0 windows for (a) OOOO′−5W−C6 and (b) OOOO′−7W−C6 simulations.

2.1.2). Subjecting the equilibrated protonated and deprotonated (λ = 0.0 or 1.0) states from the seven-water simulations to GCMC equilibration (μ_{ex} = −5.8 kcal/mol) results in the loss of the two extra added waters, indicating that the five-water configuration is more stable. However, in light of the uncertainty in μ_{ex} values in the hydrophobic interior of proteins, the existence of seven waters in the hydrophobic cavity cannot be completely ruled out.

2.2.4. Effect of the Cu$_B$ Ligation State. During the catalytic cycle of CcO, Cu$_B$ in the active site undergoes changes in both oxidation (I/II) and ligation states. For example, during the P$_R$ to F transition, it is believed that the Cu$_B$ -bound hydroxide in the P$_R$ state (OOOO) accepts a proton from Glu286 to form the F state (OOOO′) with a Cu$_B$-bound water. This alters the net charge in the active site region which in turn perturbs the electrostatic field around Glu286 and therefore its pK_a. To explore the magnitude of the perturbation, we calculate the pK_a of Glu286 with Cu$_B$-bound hydroxide (OOOO) using two independent sets of simulations and compare it to that of the OOOO′ state; the only difference between the two setups is the net charge in the active site, which changes from 0 (OOOO′) to −1 (OOOO).

As shown in Table 4, the pK_a of Glu286 increases by 3.4−4.4 pK_a units (4.5−4.9 with B3LYP correction) when the ligation state of Cu$_B$ is changed from H_2O to OH^-, which is in a reasonable range considering the distance (10.4 Å) between the two sites; i.e., the pK_a shift approximately corresponds to an effective dielectric constant of 5.8, which seems reasonable for the protein interior. Comparision of the free energy derivatives in the two cases (Table 5) shows that the increased negative charge in the OOOO state preferentially destabilizes λ windows with considerable negative charge buildup on Glu286 (λ = 0.5, 0.75, and 1.0), resulting in the observed upshift in pK_a.

The calculated pK_a shift is larger than the related results on the basis of continuum electrostatics calculations. In the work of Song et al. (*11*), the calculated pK_a for Glu286 increases from 9.7 to 11.2 upon reduction of the BNC, which corresponds to a shift of 1.6 pK_a units. The change in the charge distribution between the two redox states in their calculations, however, is rather complex: in their fully oxidized state, Cu$_B$ is predicted to bind a hydroxide while

heme$_{a3}$ binds a water; upon reduction, Cu_B binds a water while heme$_{a3}$ binds a hydroxide. Therefore, although the net charge of BNC decreases by 1 as in the OOOO′ to OOOO transition studied here, the detailed charge redistribution is more complex and might explain the differences in the computed pK_a shifts.

As stressed in section 1.1.1, Tyr288 is treated as charge-neutral in the current work to be consistent with recent MCCE calculations (*11*). This choice is also consistent with the observation that the side chain oxygen in Tyr288 is close (<3 Å) to the carbonyl in the farnesyl chain of heme$_{a3}$ in two independent X-ray structures [PDB entry 1M56 (*7*) for *R. sphaeroides* and PDB entry 1V54 (*94*) for bovine heart], therefore unlikely favoring a negatively charged state unless conformational changes occur. Nevertheless, several recent IR studies (*42, 43*) have pointed out evidence that Tyr288 is deprotonated and charge-negative in the P_R state. Clearly, additional pK_a calculations using different protonation states for Tyr288 are valuable.

2.2.5. Effect of the His334 Protonation State. Recent continuum electrostatics pK_a calculations (*39, 40*) and earlier work by Wikstrom et al. (*95*) have postulated the involvement of His334, one of the ligands of Cu_B, in the proton pumping process. This is supported by recent calculations of Stuchebrukhov et al. (*39, 40*), who predicted the His334 (*20*) protonation state to be strongly coupled to the oxidation state of the metal centers in the active site. However, recent MCCE calculations by Gunner et al. (*11*) and DFT-based continuum electrostatic pK_a calculations by Pomes et al. (*10, 96, 97*) have, on the other hand, found His334 likely to be protonated for all oxidation states of the enzyme.

An indirect way to estimate the role of His334 is to probe the sensitivity of the pK_a of Glu286 on the protonation state of His334. A change in the protonation state of His334 is likely to affect the pK_a of Glu286 due to an alteration of the total charge of the BNC in the proximity (10.2 Å). Indeed, changing only the protonation state of His334 (from 0 to −1) in the OOOO′−5w setup leads to a calculated pK_a of 18.0 (without B3LYP correction), which is ∼4.4 pK_a units higher than that of the neutral His334 state. This difference is comparable to the pK_a upshift observed for deprotonation of the Cu_B water, which is expected since both cases represent the addition of a negative charge to the BNC at similar distances from Glu286. This is reassuring with regard to the reproducibility of the challenging microscopic pK_a calculations. Interestingly, in the PB calculations of Stuchebrukov et al. (*28*), changing the protonation state of His334 also alters the pK_a of Glu286 by ∼3 units, if the dielectric constants of the protein and interior cavity are taken to be 4.0 and 15−20, respectively.

2.2.6. Effect of Protonating the Pumped Proton Loading Site (PLS). As discussed in section 1.1.1, the ligation state of Cu_B in the P_R state is uncertain. On the basis of the calculations discussed in section 2.2.3 and section 2.2.4, the combination of Cu_B-bound water and neutral His334 gives the closest agreement with the experimental pK_a of Glu286. However, on the basis of the proposed catalytic cycle (*31*), it might not be correct to assume that the P_R state has a Cu_B-bound H_2O because the Cu_B center is thought to accept a proton from Glu286 during the P_R to F transition. The experimental pK_a is estimated on the basis of the kinetics of the P_R to F transition, where the apparent pK_a reflects the fraction of CcO with a protonated Glu286 available for the proton transfer to the BNC (*24*). We note that in our model of proton pumping (*23*) as well as in recent discussions by Hummer et al. (*16, 98*), protonation of the pumped proton site precedes that of the substrate proton site; this is consistent with the experimental pK_a measurements in which the apparent kinetic value is associated with the protonation of the substrate proton site. Therefore, to characterize the fraction of "functional" Glu286 for the P_R to F transition, not only should Cu_B be bound with OH^- (OOOO state) but the PLS should be loaded with a proton. In other words, the microscopic pK_a of Glu286 ought to be calculated with the presumed PLS protonated, which may substantially lower the Glu286 pK_a with a hydroxide-bound Cu_B.

With regard to the identity of the PLS, it is commonly postulated that the Δ-propionate (PRD$_{a3}$) of heme$_{a3}$, despite being involved in salt bridge interaction with two arginines (Arg481 and Arg482), is the most likely candidate; the other propionate group, PRA$_{a3}$, has also been proposed to be the loading site (*99*), although its protonation would still require, at least transiently, protonation of PRD$_{a3}$. Mutation experiments comparing proton pumping in the R481K mutant and wild-type CcO identified a group with a pK_a of 6.3 in the wild-type enzyme, and it was assigned to the Arg481/Arg482/PRD$_{a3}$ cluster (*100*). On the other hand, continuum electrostatic calculations of Gunner et al. (*11*) using the X-ray structure predicted the pK_a of the PRD$_{a3}$ to be lower than 0 for all oxidation states (*11*), indicating that the PRD$_{a3}$ is unlikely to be protonated in the X-ray structure. However, as pointed out by many authors (*11, 101, 102*), there can be significant structural transitions in the relevant region such as breaking of the R481/R482−PRD$_{a3}$ salt bridge which would result in an increased pK_a of the PRD$_{a3}$. For example, Wikstrom and co-workers using MD simulations (*27*) have shown that the hydrogen−oxygen distance of the Arg481/PRD$_{a3}$ pair can increase to >4 Å, indicating that the ion pair can indeed dissociate. That study also showed that dissociation of the ion pair is controlled by the oxidation states of heme$_a$ and heme$_{a3}$, suggesting a redox-state dependence of the dissociation event. Following upon that work, Voth and co-workers have recently calculated the potential of mean force for PRD$_{a3}$ side chain rotation as a function of redox state and showed that the PRD$_{a3}$ can indeed reorient and dissociate from Arg481 (*93*).

Bearing those discussions in mind, we compute the Glu286 pK_a in the OOOO−5w state in the presence of a protonated PRD$_{a3}$. As shown in Table 4, the estimated pK_a for this state is 11.0 without B3LYP correction; including the B3LYP correction further reduces the pK_a to 8.1, which is fairly close to the experimental value of 9.4. We note that protonating PRD$_{a3}$ in the OOOO−5w state leads to the same net charge seen in the OOOO′−5w setup, where the Cu_B hydroxide ligand is protonated to become water. However, the calculations suggest that the pK_a of Glu286 decreases further (by ∼3 pK_a units; see Table 4) when the PRD$_{a3}$ instead of the Cu_B ligand is protonated. This difference does not seem to be a solvation effect since protonating the PRD$_{a3}$ does not induce significant changes in the solvation of Glu286 (see Figure 5). Comparing distances between the Glu286 side chains from various centers [PRD$_{a3}$, Cu_B, and Arg481(C_ζ); see Figure 6] consistently indicates that the Glu286 side chain is closer to these charged centers (especially in the $\lambda = 0.0$

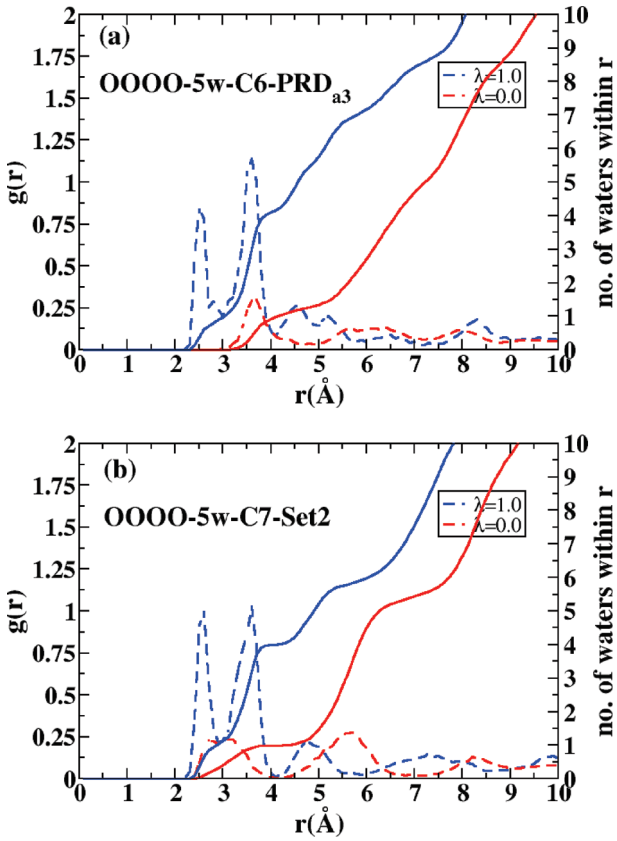

FIGURE 5: Same as Figure 4 but for (a) OOOO−5w−PRD$_{a3}$ and (b) OOOO−5w−C7 simulations.

state) when the PRD$_{a3}$ is protonated relative to when the Cu$_B$ center is protonated instead. Therefore, the lower pK_a value in the OOOO−5w−C6−PRD setup compared to that in the OOOO′−5w−C6 setup likely has an electrostatic origin.

Protonating the PRD$_{a3}$ group causes the Arg481−PRD$_{a3}$ salt bridge to break, and the distance between R481 (N_{H1}/N_{H2}) and PRD$_{a3}$ (O_{2D}/O_{1D}) fluctuates between dissociated and associated forms (Figure 7a,b), at a frequency significantly higher than when the PRD$_{a3}$ is deprotonated (Figure 7c,d). The dissociated Arg481−PRD$_{a3}$ ion pair samples two different kinds of structures. In one configuration, as shown in Figure 8a, the side chain of PRD$_{a3}$ forms a hydrogen bond with PRA$_{a3}$. Trp172, which along with PRD$_{a3}$ has been implicated (*27*) as a residue involved in gating proton release, interacts with the dissociated ion pair through hydrogen bonds either directly or via water. Interestingly, Figure 8a represents a configuration that allows the proton to be released to the P side of the membrane. Although the precise identity of the exit pathway still remains unclear, the observed structure is consistent with the predictions of continuum electrostatic calculations (*103*) and experimental studies on the E286Q (*7*) and E286H mutants (*102*), where the Arg481/Arg482−PRD$_{a3}$ salt bridge and residues around them have been implicated as a possible conduit for proton exit. In the other observed orientation (Figure 8b), the PRD$_{a3}$ side chain upon dissociation reorients itself toward the hydrophobic cavity, forming a continuous hydrogen-bonded chain with Glu286 through waters in the hydrophobic cavity. This is similar to the structure observed by Wikstrom et al. (*27*) in their MD simulations, where spontaneous dissociation of the Arg481−PRD$_{a3}$ salt bridge was observed to lead to the formation of a continuous water wire between protonated Glu286 and deprotonated PRD$_{a3}$. Although the snapshots in Figure 7 appear to indicate that the orientation of PRD$_{a3}$ is correlated with the protonation state of Glu286, multiple simulations indicate that this is not the case (data not shown).

In addition to the Arg481−PRD$_{a3}$ ion pair, the Glu286 side chain also shows considerable conformational flexibility and fluctuates between the "down" and "up" conformations as illustrated in Figure 9. Figure 10a shows the Glu286 (C_δ)−heme$_{a3}$ (O_{2D}) distance as a function of time for the deprotonated Glu286 state ($\lambda = 1.0$), which remains relatively short throughout the nanosecond scale simulation. With a protonated PRD$_{a3}$, the short separation between the deprotonated Glu286 and the protonated PRD$_{a3}$ is stable because the dissociation of the Arg481−PRD$_{a3}$ salt bridge allows the positively charged Arg481 to better stabilize the anionic Glu286; moreover, the formation of stable and continuous water chains that connect the ionized Glu286 with protonated PRD$_{a3}$ (see Figure 10b) helps maintain their proximity. This is further supported by the observation that once PRD$_{a3}$ is deprotonated, the Arg481−PRD$_{a3}$ ion pair is re-formed, which leads to disruption of the water wires to Glu286 and its downward rotation. To confirm that the observed trend is not an artifact of limited sampling, three additional simulations (~1 ns) with different seeds are carried out for the $\lambda = 1.0$ window with the OOOO−5w−C6−PRD$_{a3}$ setup. In two cases, Glu286 adopts an orientation similar to that in Figure 8b, while in the other set, Glu286 adopts a downward orientation without a continuous water wire connecting the deprotonated Glu286 to PRD$_{a3}$.

These observations hint at communication between Glu286 and PRD$_{a3}$, which may have important mechanistic implications. For example, the recent study of Hummer et al. (*16*) found that the deprotonated Glu286 strongly preferred (occurs on a picosecond scale!) the downward orientation even if the charges of PRD$_{a3}$ were set to zero to mimic protonation. Since the downward orientation of Glu286 was presumed to lack a water wire connection with PRD$_{a3}$, the observation led them to the interesting proposal that Glu286 functions as a valve to prevent leakage of protons from the P side of the membrane. By contrast, in three of four independent trajectories, we observe that protonating PRD$_{a3}$ helps stabilize the deprotonated Glu286 in an orientation in which a steady water wire connects the two groups for at least several nanoseconds. Therefore, zeroing out partial charges, which also affects PRD$_{a3}$−water interaction, is unlikely an appropriate way to investigate the effect of protonating PRD$_{a3}$. More importantly, our observations undermine the robustness of Glu286 as a valve that prevents proton leakage. Considering that the proton leakage from the P side is likely on the microsecond scale or slower, however, a more conclusive statement regarding Glu286 has to rely on a more elaborate characterization of the Glu286/PRD$_{a3}$ connectivity with free energy simulations and a protonated PRD$_{a3}$.

If Glu286 rotation is not a robust gating motion and a deprotonated Glu286 is in a steady water-mediated connection with the loaded (protonated) PRD$_{a3}$ for a sufficiently long period, what prevents proton leakage from the P side? The simulations in this work do not directly address this important mechanistic question, and we believe that the answer lies in the energetic cost associated with generating

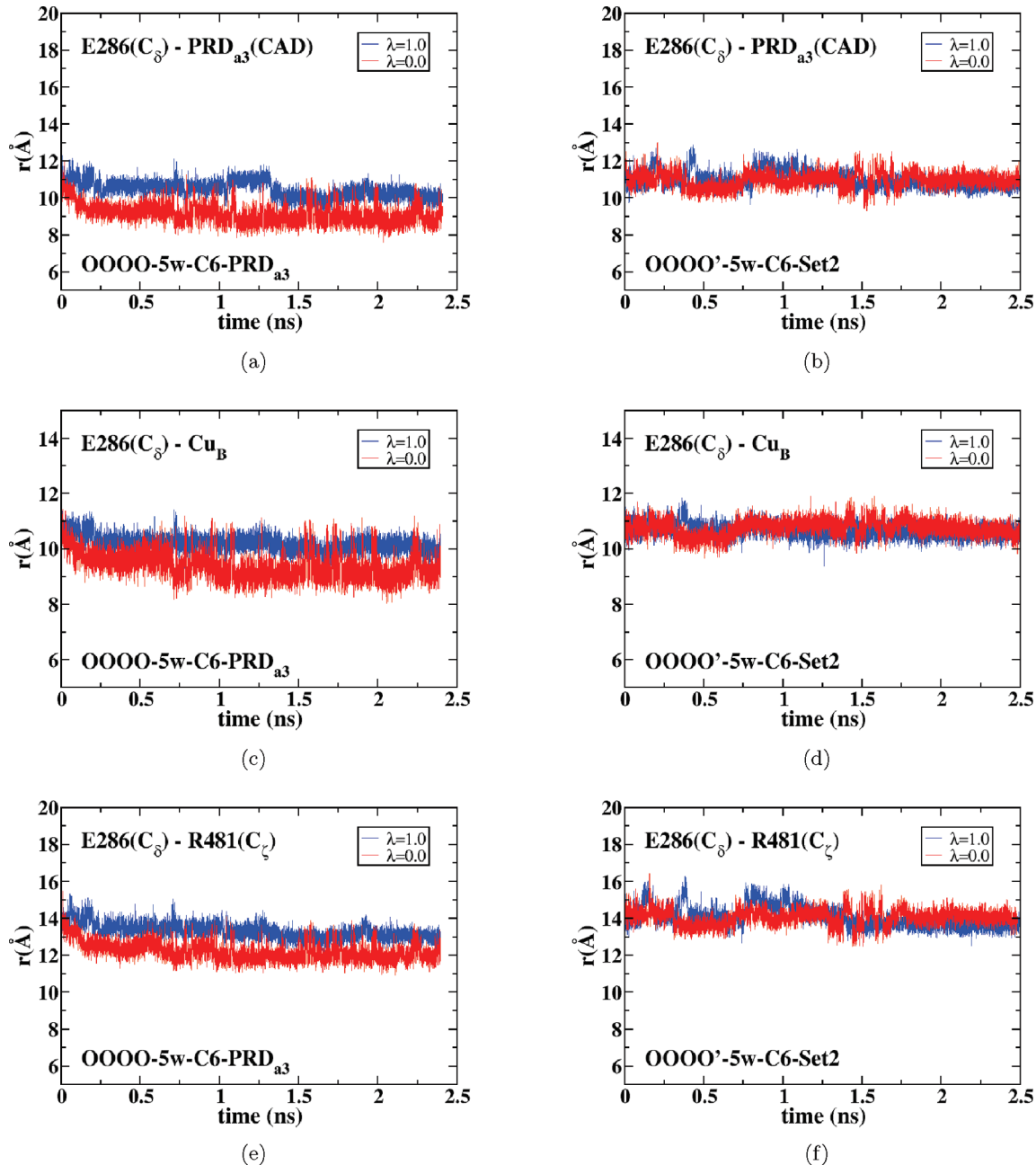

FIGURE 6: Comparison of distances between Glu286 (C_δ) and various charged centers [CAD in PRD_{a3}; see Figure 9 for label; Cu_B; Arg481 (C_ζ)] in the OOOO−5w−C6−PRD_{a3} and OOOO′−5w−C6 simulations. Note that the Glu286 side chain is consistently closer to these charged centers when the PRD_{a3} is protonated.

a hydronium-like species near or in the hydrophobic cavity, as argued by Warshel and co-workers in their recent analysis (*22*). A related question is after PRD_{a3} is loaded, what prevents the pumped proton from "falling back" to the presumably thermodynamically more favorable substrate proton site? Indeed, with a deprotonated Glu286, the protonated PRD_{a3} is also connected to the substrate proton site through a water wire (see Figure 10c). Therefore, it is likely that the key still lies in the energetic penalty associated with generating a hydronium-like species in the hydrophobic cavity; the same principle may also be responsible for the kinetic gating (i.e., proton transfer to the pumped proton loading site precedes to the substrate proton site) phenomena that several groups have suggested (*20*−*23*) as an important factor governing the pumping function of CcO. In short, answering these important mechanistic questions requires explicitly dealing with the energetics (especially barrier) of proton transfers in CcO, which will be reported separately.

3. CONCLUDING REMARKS

Proton pumping in CcO is a fascinating and complex process. Since the process is likely dependent on relatively subtle structural rearrangements of protein motifs and water molecules, detailed theoretical and computational analyses can effectively complement experimental investigations in revealing the key molecular factors that govern the pumping function. As appreciated by many authors, however, a meaningful computational analysis requires the establishment of a molecular model and computational framework that can properly describe the structure, dynamics, and, more importantly, energetics of the CcO active site.

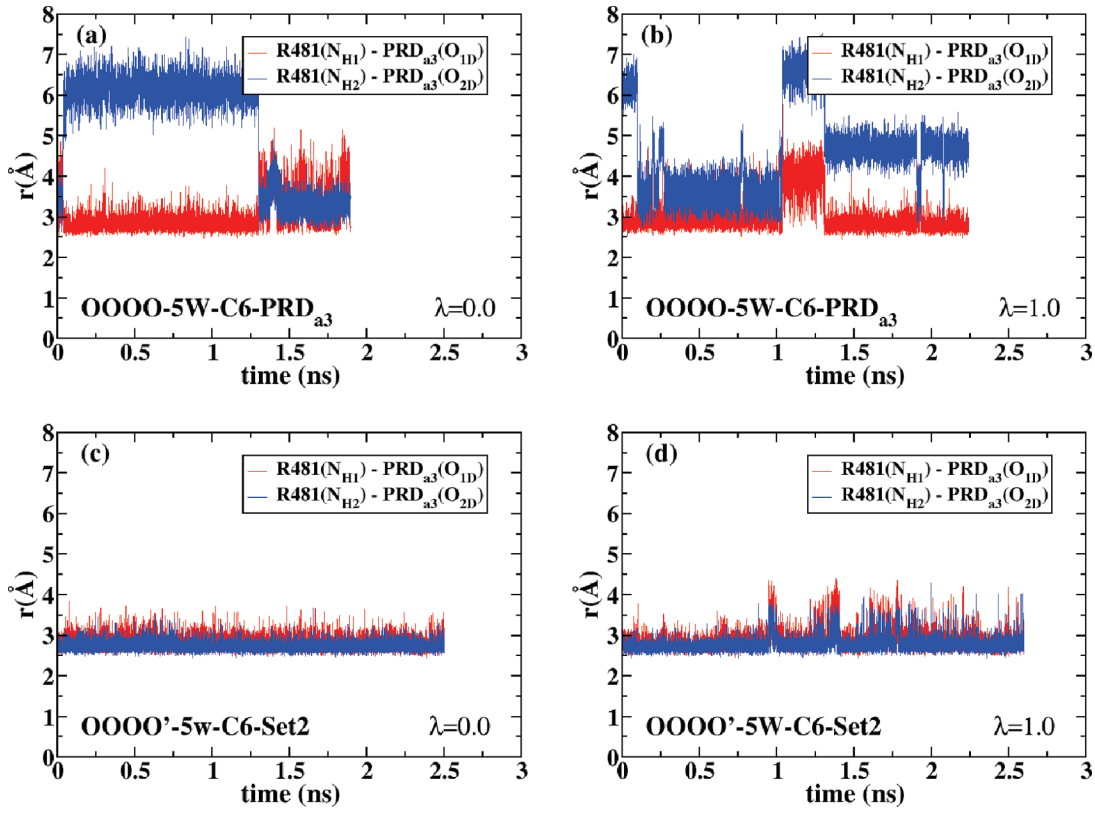

FIGURE 7: Fluctuation of the salt bridge between Arg481 and PRD_{a3} in (a and b) OOOO−5w−C6−PRD_{a3} and (c and d) OOOO′−5w−C6 simulations as indicated by the distances between the relevant H−O pairs [Arg481 (N_{H1}/N_{H2})−PRD_{a3} ($O_{2\delta}$/$O_{1\delta}$)]. As expected, the salt bridge tends to break more often as PRD_{a3} is protonated (i.e., panels a and b).

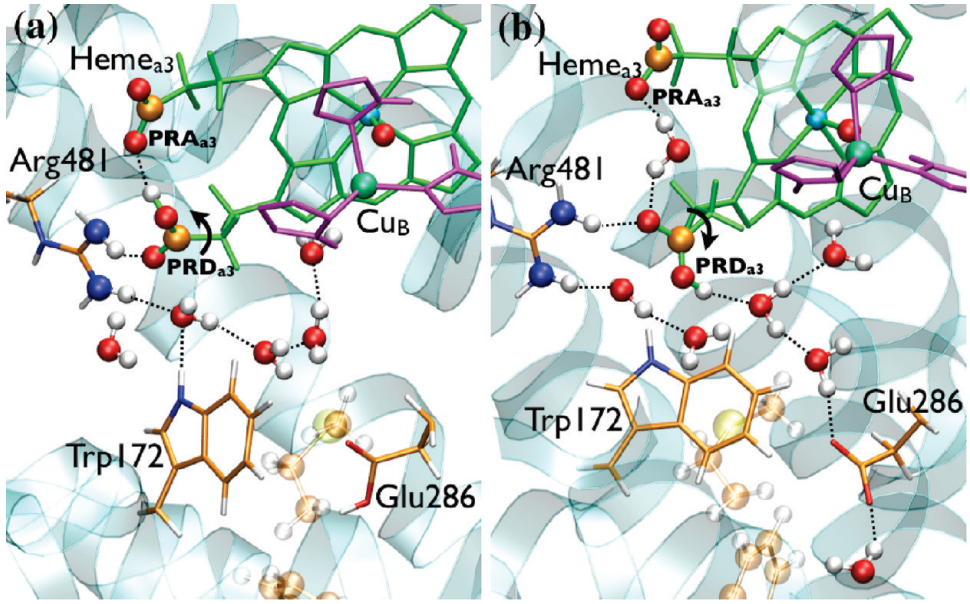

FIGURE 8: Snapshot from OOOO−5w−C6−PRD_{a3} simulations that illustrate two different orientations of the PRD_{a3} side chain: (a) an upward orientation that forms a hydrogen bond with PRA_{a3} and (b) a downward orientation that forms a continuous water wire to the deprotonated Glu286 and the chemical site (Cu_B with a hydroxide). Independent simulations show that the orientation of the PRD_{a3} is not necessarily tightly coupled to the protonation state of Glu286.

In this work, we have attempted to carefully evaluate the molecular model and our QM/MM computational protocol by computing the pK_a of the key residue, Glu286 in *R. sphaeroides* CcO. As emphasized in several studies, particularly those by us (*76, 104*) and Warshel (*105, 106*), microscopic pK_a calculations are among the most stringent and relevant tests for proton transfer problems. Specifically, we have examined the impact of the number of water molecules in the hydrophobic cavity and protonation state of several key residues on the computed microscopic pK_a value of Glu286. To help evaluate the systematic errors in our SCC-DFTB/MM-GSBP-based thermodynamic integration protocol, microscopic pK_a calculations have also been conducted for sites in a soluble protein (Asp70 in T4 lysozyme) and a better characterized membrane protein (Asp85 in bacteriorhodopsin).

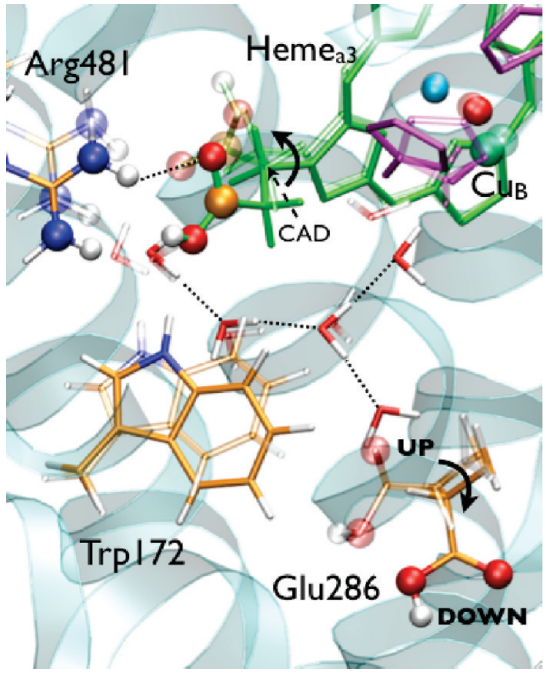

FIGURE 9: Snapshots from OOOO−5w−C6−PRD$_{a3}$ simulations that illustrate the two orientations sampled by the Glu286 side chain in different protonation states. The structure from the $\lambda = 0.0$ (protonated) state simulation is shown in opaque, while that from the $\lambda = 1.0$ (deprotonated) window is shown in a transparent representation. Independent simulations indicate that the orientation of the Glu286 side chain is not only controlled by its protonation state but also more sensitive to the protonation state of PRD$_{a3}$.

There are several useful conclusions from this study. First, although it is acknowledged that microscopic pK_a calculations are generally highly challenging, especially concerning the degree of sampling (*53, 107*) and treatment of long-range electrostatics (including polarization) (*105*), the results obtained here show a significant degree of internal consistency that support the effectiveness of the computational framework. For example, the pK_a shift of Glu286 is similar when either the water or His334 of Cu$_B$ is deprotonated, which is consistent with the fact that these two groups have a similar distance separation from Glu286; protonating PRD$_{a3}$ helps bring the deprotonated Glu286 closer, which is in line with the larger pK_a shift compared to changing the charge state of Cu$_B$ ligands. In cases where multiple independent simulations are carried out, the computed pK_a values are usually within 0.5−0.8 pK_a unit.

Second, with a careful treatment of the QM/MM interaction, the number of water molecules in the hydrophobic cavity (five vs seven) has a relatively small impact on the microscopic pK_a of Glu286, which is consistent with the idea that the pK_a of Glu286 should not fluctuate dramatically as water molecules keep being produced during the functional cycle. More importantly, however, the protonation state of several residues, some of which can be rather far away, has a more important impact on the pK_a of Glu286, implying limited screening in membrane protein systems. Adopting the standard protonation state for all titratable residues leaves a large net charge on the system and also a significantly elevated pK_a for Glu286 beyond the expected error range of

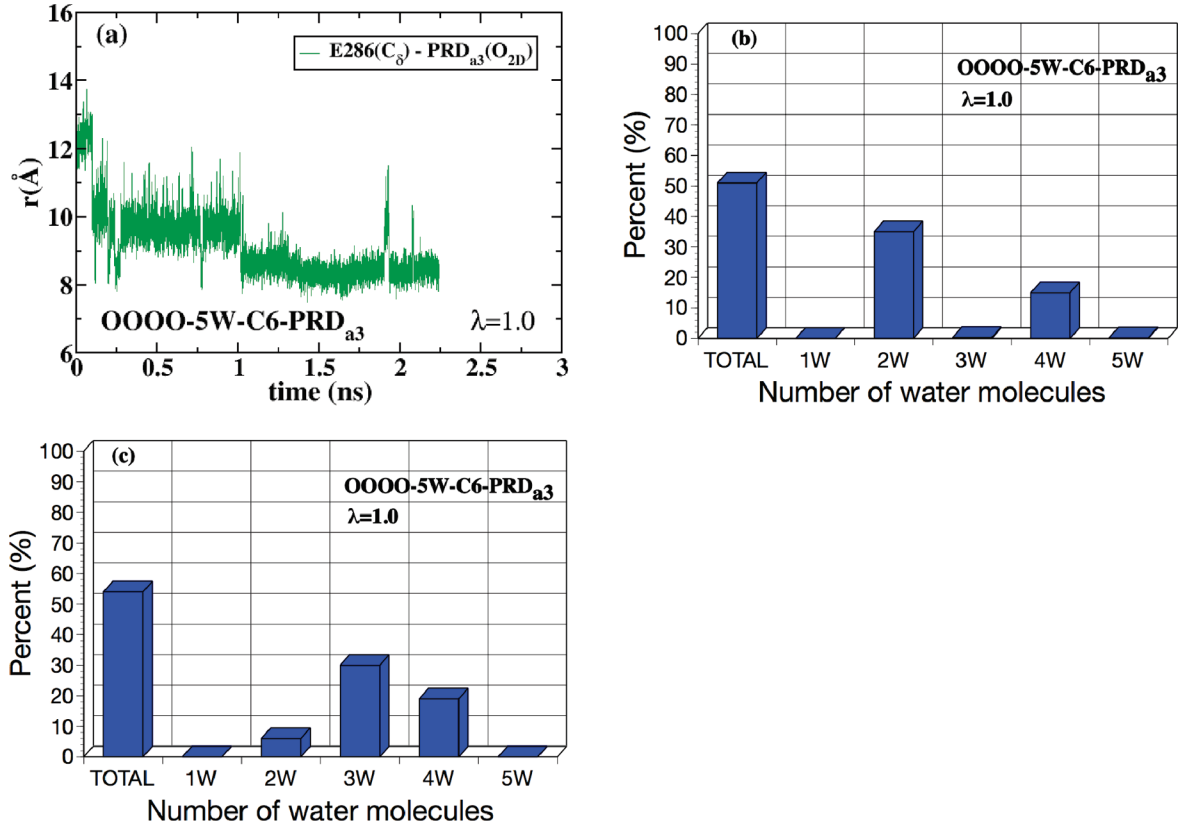

FIGURE 10: Properties that characterize the connection between the protonated PRD$_{a3}$ and Glu286/Cu$_B$ in the $\lambda = 1.0$ (deprotonated Glu286) window of OOOO−5W−C6−PRD$_{a3}$ simulations. (a) Distance between Glu286 (C$_\delta$) and PRD$_{a3}$ (O$_{2D}$), which was used in ref *16* to characterize the up or down orientation of Glu286. (b) Percentage of trajectory frames that contain a productive water wire between protonated PRD$_{a3}$ and Glu286 (O$_{\epsilon 2}$). The distribution of water wires of different lengths is also shown. (c) Same data for the connection between PRD$_{a3}$ and the OH ligand of Cu$_B$. The algorithm for determining the water wire distribution follows from our recent studies of proton transfers in carbonic anhydrase (*30, 76, 104, 109*).

our computational protocol. Therefore, any attempt to address the energetics of proton transfers in CcO at a microscopic level should carefully select the protonation state of residues, even those not in the immediate neighborhood of the active site. Along this line, combining continuum electrostatic models and microscopic models, as we have done here, is a productive avenue.

Third, although we have not explicitly calculated the redox-dependent pK_a of His334, the computed pK_a of Glu286 with a negatively charged His334 is very high even with an oxidized Cu_B and a water ligand. If one argues that the relevant state should include a protonated PRD_{a3} and Cu_B hydroxide, the trends in Table 4 would still point to a pK_a for Glu286 that is too high compared to the experimental value. Therefore, our calculations indirectly suggest that His334 is unlikely to become deprotonated (charge-negative) in the pumping cycle.

Last but certainly not the least, we find that the orientation of the Glu286 side chain is coupled to the protonation state of PRD_{a3}, the presumed pumped proton loading site. With a protonated PRD_{a3}, the deprotonated Glu286 is in a steady water wire connection with PRD_{a3} for at least several nanoseconds due to the electrostatic stabilization provided by Arg481 following its dissociation from PRD_{a3}. This observation highlights the importance of explicitly protonating PRD_{a3} for studying its conformational coupling with Glu286 and, more importantly, undermines the robustness of Glu286 as a gating valve that prevents proton leakage (*16*).

Ultimately, answering key mechanistic questions about proton pumping in CcO, such as factors that govern kinetic gating (*20*−*23*) and prevent proton leakage (*16, 19, 22*), requires detailed analysis of proton transfer kinetics. The microscopic analysis performed here has provided useful guidance to the development of a meaningful molecular model for this complex system. The large sets of calculations also help validate the QM/MM-GSBP-based computational framework for addressing the structural and energetic features of the CcO active site. Although additional benchmark calculations should be done with, for example, a different MM parametrization for the cofactors ($heme_a$, $heme_{a3}$, and Cu_B) (*108*) and different protonation states of Tyr288 (*42, 43*) and the other emerging candidate for the loading site (PRA_{a3}) (*99*), we believe that the stage is set for detailed analyses of various proton transfer pathways and, in turn, disclosure of molecular features of CcO that make it one of the most fascinating ion pumps in biology.

ACKNOWLEDGMENT

We thank Dr. Y. Song for valuable discussions regarding both bR and CcO calculations using the MCCE approach. Computational resources from the National Center for Supercomputing Applications at the University of Illinois are greatly appreciated.

SUPPORTING INFORMATION AVAILABLE

Force field parameters developed for the metal centers. This material is available free of charge via the Internet at http://pubs.acs.org.

REFERENCES

1. Brzezinski, P. (2004) Redox-driven membrane-bound proton pumps. *Trends Biochem. Sci. 29*, 380–387.
2. Brzezinski, P., and Larsson, G. (2003) Redox-driven membrane-bound proton pumps. *Biochim. Biophys. Aca 1605*, 1–13.
3. Ferguson-Miller, S., and Babcock, G. T. (1996) Heme/copper terminal oxidases. *Chem. Rev. 96*, 2889–2907.
4. Hosler, J. P., Ferguson-Miller, S., and Mills, D. A. (2006) Energy transduction: Proton transfer through the respiratory complexes. *Annu. Rev. Biochem. 75*, 165–187.
5. Wikstrom, M. (1998) Proton translocation by bacteriorhodopsin and heme-copper oxidases. *Curr. Opin. Struct. Biol. 8*, 480.
6. Yoshikawa, S., Shinzawa-Itoh, K., Nakashima, R., Yaono, R., Yamashita, E., Inoue, N., Yao, M., Fei, M. J., Libeu, C. P., Mizushima, T., Yamaguchi, H., Tomizaki, T., and Tsukihara, T. (1998) Redox-coupled crystal structural changes in bovine heart cytochrome c oxidase. *Science 280*, 1723–1729.
7. Svensson-Ek, M., Abramson, J., Larsson, G., Tornroth, S., Brzezinski, P., and Iwata, S. (2002) The X-ray crystal structures of wild-type and EQ(I-286) mutant cytochrome c oxidases from *Rhodobacter sphaeroides*. *J. Mol. Biol. 321*, 329.
8. Kannt, M. H. A., and Lancaster, C. R. (1998) The coupling of electron transfer and proton translocation: Electrostatic calculations on *Paracoccus denitrificans* cytochrome c oxidase. *Biophys. J. 74*, 708–721.
9. Popovic, D. M., and Stuchebrukhov, A. A. (2004) Electrostatic study of the proton pumping mechanism in bovine heart cytochrome c oxidase. *J. Am. Chem. Soc. 126*, 1858–1871.
10. Fadda, E., Chakrabarti, N., and Pomes, R. (2005) Acidity of a Cu-bound histidine in the binuclear center of cytochrome c oxidase. *J. Phys. Chem. B 109*, 22629–22640.
11. Song, Y., Michonova-Alexova, E., and Gunner, G. M. (2006) Calculated proton uptake on anaerobic reduction of cytochrome c oxidase: Is the reaction electroneutral? *Biochemistry 45*, 7959.
12. Fadda, E., Yu, C.-H., and Pomes, R. (2008) Electrostatic control of proton pumping in cytochrome c oxidase. *Biochim. Biophys. Acta 1777*, 277–284.
13. Olkhova, E., Hutter, M., Lill, M., and Helms, V. H. M. H. (2004) Dynamic water networks in cytochrome c oxidase from *Paracoccus denitrificans* investigated by molecular dynamics simulations. *Biophys. J. 86*, 1873–1889.
14. Xu, J., and Voth, G. A. (2005) Computer simulation of explicit proton translocation in cytochrome c oxidase: The D-pathway. *Proc. Natl. Acad. Sci. U.S.A. 102*, 6795–6800.
15. Xu, J., and Voth, G. A. (2006) Free energy profile for H^+ conduction in the D-pathway of cytochrome c oxidase: A study of the wild type and N98D mutant enzymes. *Biochim. Biophys. Acta 1757*, 852–859.
16. Kaila, V. R. I., Verkhovsky, M. I., Hummer, G., and Wikstrom, M. (2008) Glutamic acid 242 is a valve in the proton pump of cytochrome c oxidase. *Proc. Natl. Acad. Sci. U.S.A. 105* (17), 6255.
17. Siegbahn, P. E. M., Blomberg, M. R. A., and Blomberg, M. L. (2003) Theoretical study of the energetics of proton pumping and oxygen reduction in cytochrome c oxidase. *J. Phys. Chem. B 107*, 10946–10955.
18. Blomberg, M. R. A., and Siegbahn, P. E. M. (2006) Different types of biological proton transfer reactions studied by quantum chemical methods. *Biochim. Biophys. Acta 1757*, 969–980.
19. Siegbahn, P. E. M., and Blomberg, M. R. A. (2007) Energy diagrams and mechanism for proton pumping in cytochrome c oxidase. *Biochim. Biophys. Acta 1767*, 1143–1156.
20. Popovic, D. M., and Stuchebrukhov, A. S. (2004) Proton pumping mechanism and catalytic cycle of cytochrome c oxidase: Coulomb pump model with kinetic gating. *FEBS Lett. 566*, 126.
21. Olsson, M. H. M., and Warshel, A. (2006) Monte carlo simulations of proton pumps: On the working principles of the biological valve that controls proton pumping in cytochrome c oxidase. *Proc. Natl. Acad. Sci. U.S.A. 103* (17), 6500.
22. Pisliakov, A. V., Sharma, P. K., Chu, Z. T., Haranczyk, M., and Warshel, A. (2008) Electrostatic basis for the unidirectionality of the primary proton transfer in cytochrome c oxidase. *Proc. Natl. Acad. Sci. U.S.A. 105*, 7726–7731.
23. Cui, Q. (2006) Theoretical and computational studies of vectorial processes in biological systems. *Theor. Chem. Acc. 116* (New Perspectives in Theoretical Chemistry), 51–59.
24. Namslauer, A., Aagaard, A., Katsonouri, A., and Brzezinski, P. (2003) Intramolecular proton-transfer reactions in a membrane-bound proton pump: The effect of pH on the peroxy to ferryl transition in cytochrome c oxidase. *Biochemistry 42*, 1488.

25. Riistama, S., Hummer, G., Puustinen, A., Dyer, R. B., Woodruff, W. H., and Wikstrom, M. (1997) Bound water in the proton translocation mechanism of the haem-copper oxidases. *FEBS Lett. 414*, 275.
26. Wikstrom, M., Verkhovsky, M. I., and Hummer, G. (2003) Water-gated mechanism of proton translocation by cytochrome c oxidase. *Biochim. Biophys. Acta 1604*, 61.
27. Wikstrom, M., Ribacka, C., Molin, M., Laakonnen, L., Verkhovsky, M. I., and Puustinen, A. (2005) Gating of proton and water transfer in the respiratory enzyme cytochrome c oxidase. *Proc. Natl. Acad. Sci. U.S.A. 102*, 10478.
28. Popovic, D. M., and Stuchebrukhov, A. A. (2006) Two conformational states of glu242 and pK_as in bovine cytochrome c oxidase. *Photochem. Photobiol. Sci. 5*, 611–620.
29. Riccardi, D., Schaefer, P., and Cui, Q. (2005) pK_a calculations in solution and proteins with QM/MM free energy perturbation simulations. *J. Phys. Chem. B 109*, 17715–17733.
30. Riccardi, D., Schaefer, P., Yang, Y., Yu, H., Ghosh, N., Prat-Resina, X., König, P., Li, G., Xu, D., Guo, H., Elstner, M., and Cui, Q. (2006) Development of effective quantum mechanical/molecular mechanical (QM/MM) methods for complex biological processes. *J. Phys. Chem. B 110*, 6458–6469.
31. Bränden, G., Gennis, R. B., and Brzezinski, P. (2006) Transmembrane proton translocation by cytochrome c oxidase. *Biochim. Biophys. Acta 1757*, 1052–1063.
32. Li, G., and Cui, Q. (2003) pK_a calculations with QM/MM free energy perturbations. *J. Phys. Chem. B 107*, 14521–14528.
33. Schaefer, P., Riccardi, D., and Cui, Q. (2005) Reliable treatment of electrostatics in combined QM/MM simulation of macromolecules. *J. Chem. Phys. 123*, 014905.
34. Zheng, X., Medvedev, D. M., Swanson, J., and Stuchebrukhov, A. A. (2003) Computer simulation of water in cytochrome c oxidase. *Biochim. Biophys. Acta 1557*, 99–107.
35. Tashiro, M., and Stuchebrukhov, A. A. (2005) Thermodynamic properties of internal water molecules in the hydrophobic cavity around the catalytic center of cytochrome c oxidase. *J. Phys. Chem. B 109*, 1015–1022.
36. Woo, H. J., Dinner, A. R., and Roux, B. (2004) Grand canonical monte carlo simulations of water in protein environments. *J. Chem. Phys. 121*, 6392–6400.
37. Tuukkanena, A., Kailaa, V. R., Laakkonena, L., Hummerb, G., and Wikström, M. (2007) Dynamics of the glutamic acid 242 side chain in cytochrome c oxidase. *Biochim. Biophys. Acta 1767* (9), 1102–1106.
38. Jorgensen, W. L., Chandrasekhar, J., Madura, J. D., Impey, R. W., and Klein, M. L. (1983) Comparison of simple potential functions for simulating liquid water. *J. Chem. Phys. 79*, 926.
39. Popovic, D. M., Quenneville, J., and Stuchebrukhov, A. A. (2005) DFT/electrostatic calculations of pK_a values in cytochrome c oxidase. *J. Phys. Chem. B 109*, 3616–3626.
40. Quenneville, J., Popovic, D. M., and Stuchebrukhov, A. A. (2006) Combined dft and electrostatics study of the proton pumping mechanism in cytochrome c oxidase. *Biochim. Biophys. Acta 1757*, 1035–1046.
41. Makhov, D. V., Popovic, D. M., and Stuchebrukhov, A. A. (2006) Improved density functional theory/electrostatic calculation of the his291 protonation state in cytochrome c oxidase: Self-consistent charges for solvation energy calculation. *J. Phys. Chem. B 110*, 12162–12166.
42. Gorbikova, E. A., Wikström, M., and Verkhovsky, M. I. (2008) The protonation state of the cross-linked tyrosine during the catalytic cycle of cytochrome c oxidase. *J. Biol. Chem. 283*, 34907–34912.
43. Gorbikova, E. A., Belevich, I., Wikström, M., and Verkhovsky, M. I. (2008) The proton donor for O−O bond scission by cytochrome c oxidase. *Proc. Natl. Acad. Sci. U.S.A. 105*, 10733–10737.
44. Im, W., Bernéche, S., and Roux, B. (2001) Generalized solvent boundary potential for computer simulations. *J. Chem. Phys. 114* (7), 2924–2937.
45. Schaefer, P., Riccardi, D., and Cui, Q. (2005) Reliable treatment of electrostatics in combined QM/MM simulation of macromolecules. *J. Chem. Phys. 123*, 14905.
46. Rychaert, J. P., Ciccotti, G., and Berendsen, H. J. (1977) Numerical integration of the cartesian equations of motion of a system with constraints: Molecular dynamics of n-alkanes. *J. Comput. Phys. 23*, 327–341.
47. Frenkel, D., and Smit, B. (1996) *Understanding Molecular Simulations: From Algorithms to Applications*, Academic Press, San Diego.
48. König, P., Ghosh, N., Hoffman, M., Elstner, M., Tajkhorshid, E., Frauenheim, T., and Cui, Q. (2006) Towards theoretical analysis of long-range proton transfer kinetics in biomolecular pumps. *J. Phys. Chem. A 110*, 548–563.
49. Nina, M., and Roux, B. (1997) Atomic radii for continuum electrostatics calculations based on molecular dynamics free energy simulations. *J. Phys. Chem. B 101*, 5239–5248.
50. Stote, R. S. D. J., and Karplus, M. (1991) On the treatment of electrostatics interactions in biomolecular simulations. *J. Chim. Phys. 88*, 2419.
51. MacKerell, A. D., Jr. (1998) All-atom empirical potential for molecular modeling and dynamics studies of proteins. *J. Phys. Chem. B 102*, 3586–3616.
52. Koenig, P., Hoffmann, M., Frauenheim, T., and Cui, Q. (2005) A critical evaluation of different QM/MM frontier treatments with SCC-DFTB as the QM method. *J. Phys. Chem. B 109*, 9082–9095.
53. Ghosh, N., and Cui, Q. (2008) pK_a of residue 66 in *staphylococal nuclease*: Insights from QM/MM simulations with conventional sampling. *J. Phys. Chem. B 112*, 8387–8397.
54. Becke, A. D. (1993) Density-functional thermochemistry. III. The role of exact exchange. *J. Chem. Phys. 98* (7), 5648–5652.
55. Becke, A. D. (1988) Density-functional exchange-energy approximation with correct asymptotic behavior. *Phys. Rev. A 38*, 3098–3100.
56. Hay, P. J., and Wadt, W. R. (1985) Ab initio effective core potentials for molecular calculations. Potentials for the transition metal atoms Sc to Hg. *J. Chem. Phys. 82* (1), 270–283.
57. Wadt, W. R., and Hay, P. J. (1985) Ab initio effective core potentials for molecular calculations. Potentials for main group elements Na to Bi. *J. Chem. Phys. 82* (1), 284–298.
58. Hay, P. J., and Wadt, W. R. (1985) Ab initio effective core potentials for molecular calculations. Potentials for K to Au including the outermost core orbitals. *J. Chem. Phys. 82* (1), 299–310.
59. Frisch, M. J., Pople, J. A., and Binkley, J. S. (1984) Self-consistent molecular-orbital methods. 25. Supplementary functions for Gaussian-basis sets. *J. Chem. Phys. 80*, 3265–3269.
60. Frisch, M. J., Trucks, G. W., Schlegel, H. B., Scuseria, G. E., Robb, M. A., Cheeseman, J. R., Montgomery, J. A., Jr., Vreven, T., Kudin, K. N., Burant, J. C., Millam, J. M., Iyengar, S. S., Tomasi, J., Barone, V., Mennucci, B., Cossi, M., Scalmani, G., Rega, N., Petersson, G. A., Nakatsuji, H., Hada, M., Ehara, M., Toyota, K., Fukuda, R., Hasegawa, J., Ishida, M., Nakajima, T., Honda, Y., Kitao, O., Nakai, H., Klene, M., Li, X., Knox, J. E., Hratchian, H. P., Cross, J. B., Bakken, V., Adamo, C., Jaramillo, J., Gomperts, R., Stratmann, R. E., Yazyev, O., Austin, A. J., Cammi, R., Pomelli, C., Ochterski, J. W., Ayala, P. Y., Morokuma, K., Voth, G. A., Salvador, P., Dannenberg, J. J., Zakrzewski, V. G., Dapprich, S., Daniels, A. D., Strain, M. C., Farkas, O., Malick, D. K., Rabuck, A. D., Raghavachari, K., Foresman, J. B., Ortiz, J. V., Cui, Q., Baboul, A. G., Clifford, S., Cioslowski, J., Stefanov, B. B., Liu, G., Liashenko, A., Piskorz, P., Komaromi, I., Martin, R. L., Fox, D. J., Keith, T., Al-Laham, M. A., Peng, C. Y., Nanayakkara, A., Challacombe, M., Gill, P. M. W., Johnson, B., Chen, W., Wong, M. W., Gonzalez, C., and Pople, J. A. (2004) Gaussian03, Revision c.02, Gaussian, Inc., Wallingford, CT.
61. Singh, U. C., and Kollman, P. A. (1984) An approach to computing electrostatic charges for molecules. *J. Comput. Chem. 5*, 129–145.
62. Besler, B. H., Merz, K. M., Jr., and Kollman, P. A. (1990) Atomic charges derived from semiempirical methods. *J. Comput. Chem. 11*, 431–439.
63. Krishnan, R., Binkley, J. S., Seeger, R., and Pople, J. A. (1980) Self-consistent molecular-orbital methods. 20. Basis set for correlated wave-functions. *J. Chem. Phys. 72* (1), 650–654.
64. Dao-pin, S., Anderson, D. E., Baase, W. A., Dahlquist, F. W., and Matthews, B. W. (1991) Structural and thermodynamic consequences of burying a charged residue within the hydrophobic core of T4 lysozyme. *Biochemistry 30*, 11521–11529.
65. Luecke, H., Schobert, B., Richter, H. T., Cartailler, J. P., and Lanyi, J. K. (1999) Structure of bacteriorhodopsin at 1.55 Å resolution. *J. Mol. Biol. 291*, 899–911.
66. Balashov, S. (2000) Protonation reactions and their coupling in bacteriorhodopsin. *Biochim. Biophys. Acta 1469*, 75–95.

67. Tajkhorshid, E., and Suhai, S. (1999) Influence of methyl groups on the structure, charge distribution and proton affinity of the retinal Schiff base. *J. Phys. Chem. B 103*, 5581.
68. Tajkhorshid, E., Paizs, B., and Suhai, S. (1999) Role of isomerization barriers in the pK_a control of the retinal Schiff base. *J. Phys. Chem. B 103*, 4518.
69. Song, Y. F., Mao, J. J., and Gunner, M. (2003) Calculation of proton transfers in bacteriorhodopsin BR and M intermediates. *Biochemistry 42*, 9875–9888.
70. Straatsma, T. P., and McCammon, J. A. (1992) Computational alchemy. *Annu. Rev. Phys. Chem. 43*, 407–435.
71. Kollman, P. (1993) Free energy calculations. *Chem. Rev. 93*, 2395–2417.
72. Lide, D. R. (2005) *CRC Handbook Chemistry and Physics*, 85th ed., CRC Press, Boca Raton, FL.
73. Simonson, T. (2002) Gaussian fluctuations and linear response in an electron transfer protein. *Proc. Natl. Acad. Sci. U.S.A. 99*, 6544–6549.
74. Levy, R., Belhadj, M., and Kitchen, D. (1991) Gaussian fluctuation formula for electrostatic free energy changes. *J. Chem. Phys. 95*, 3627–3633.
75. Simonson, T., Carlsson, J., and Case, D. A. (2004) Proton binding to proteins: pK_a calculations with explicit and implicit solvent models. *J. Am. Chem. Soc. 126*, 4167.
76. Riccardi, D., and Cui, Q. (2007) pK_a analysis for the zinc-bound water in human carbonic anhydrase. II. Benchmark for "multiscale" QM/MM simulations and mechanistic implications. *J. Phys. Chem. A 111*, 5703–5711.
77. Cui, Q., Elstner, M., Kaxiras, E., Frauenheim, T., and Karplus, M. (2001) A QM/MM implementation of the self consistent charge density functional tight binding (SCC-DFTB) method. *J. Phys. Chem. B 105* (2), 569–585.
78. Elstner, M., Porezag, D., Jungnickel, G., Elstner, J., Haugk, M., Frauenheim, T., Suhai, S., and Seifert, G. (1998) Self-consistent-charge density-functional tight-binding method for simulations of complex materials properties. *Phys. Rev. B 58* (11), 7260–7268.
79. Lyne, P. D., Hodoscek, M., and Karplus, M. (1999) A hybrid QM-MM potential employing Hartree-Fock or density functional methods in the quantum region. *J. Phys. Chem. A 103*, 3462–3471.
80. Štrajbl, M., Hong, G., and Warshel, A. (2002) Ab initio QM/MM simulation with proper sampling: "First principle" calculations of the free energy of the autodissociation of water in aqueous solution. *J. Phys. Chem. B 106*, 13333–13343.
81. Elstner, M., Frauenheim, T., and Suhai, S. (2003) An approximate DFT method for QM/MM simulations of biological structures and processes. *THEOCHEM 632*, 29.
82. Otte, N., Scholten, M., and Thiel, W. (2007) Looking at self-consistent-charge density functional tight binding from a semiempirical perspective. *J. Phys. Chem. A 111*, 5751–5755.
83. Anderson, D. E., Becktel, W. J., and Dahlquist, F. W. (1990) pH-induced denaturation of proteins: A single salt bridge contributes 3−5 kcal/mol to the free energy of folding in T4 lysozyme. *Biochemistry 29*, 2403–2408.
84. Li, H., Hains, A. W., Everts, J. E., Robertson, A. D., and Jensen, J. H. (2002) The prediction of protein pK_a's using QM/MM: The pK_a of lysine 55 in turkey ovomucoid third domain. *J. Phys. Chem. B 106*, 3486–3494.
85. Schultz, C. N., and Warshel, A. (2001) What are the dielectric constants of proteins and how to validate electrostatic models. *Proteins 44*, 400.
86. Luecke, H., and Lanyi, J. K. (2003) Structural clues to the mechanism of ion pumping in bacteriorhodopsin. *Adv. Protein Chem. 63*, 111–130.
87. Garczarek, F., Brown, L. S., Lanyi, J. K., and Gerwert, K. (2005) Proton binding within a membrane protein by a protonated water cluster. *Proc. Natl. Acad. Sci. U.S.A. 102*, 3633–3638.
88. Mathias, G., and Marx, D. (2007) Structures and spectral signatures of protonated water networks in bacteriorhodopsin. *Proc. Natl. Acad. Sci. U.S.A. 104*, 6980–6985.
89. Phatak, P., Ghosh, N., Yu, H., Cui, Q., and Elstner, M. (2008) Amino acids with an intermolecular proton bond as proton storage site in bacteriorhodopsin. *Proc. Natl. Acad. Sci. U.S.A. 105*, 19672–19677.
90. Lubben, M., Prutsch, A., Mamat, B., and Gerwert, K. (1999) Electron transfer induces side-chain conformational changes of glutamate-286 from cytochrome bo3. *Biochemistry 38*, 2048.
91. Gorbikova, E. A., Belevich, N. P., Wikström, M., and Verkhovsky, M. I. (2007) Protolytic reactions on reduction of cytochrome c oxidase studied by ATR-FTIR spectroscopy. *Biochemistry 46*, 4177.
92. Xu, J., Sharpe, M. A., Qin, L., Ferguson-Miller, S., and Voth, G. A. (2007) Storage of an excess proton in the hydrogen-bonded network of the D pathway of cytochrome c oxidase: Identification of a protonated water cluster. *J. Am. Chem. Soc. 129*, 2910–2913.
93. Xu, J., and Voth, G. A. (2008) Redox-coupled proton pumping in cytochrome c oxidase: Further insights from computer simulation. *Biochim. Biophys. Acta 1777*, 196.
94. Tsukihara, T., Shimokata, K., Katayama, Y., Shimada, H., Muramoto, K., Aoyama, H., Mochizuki, M., Shinzawa-Itoh, K., Yamashita, E., Yao, M., Ishimura, Y., and Yoshikawa, S. (2003) The low-spin heme of cytochrome c oxidase as the driving element of the proton-pumping process. *Proc. Natl. Acad. Sci. U.S.A. 100*, 15304–15309.
95. Wikstrom, M., Bogachev, A., Finel, M., Morgan, J. E., Puustinen, A., Raitio, M., Verkhovskaya, M., and Verkhovskaya, M. I. (1994) Mechanism of proton translocation by the respiratory oxidases: The histidine cycle. *Biochim. Biophys. Acta 1187*, 106–111.
96. Stuchebrukhov, A. A., and Popovic, D. M. (2006) Comment on "acidity of a Cu-bound histidine in the binuclear center of cytochrome c oxidase". *J. Phys. Chem. B 110*, 17286–17287.
97. Fadda, E., Chakrabarti, N., and Pomes, R. (2006) Reply to "comment on acidity of a Cu-bound histidine in the binuclear center of cytochrome c oxidase". *J. Phys. Chem. B 110*, 17288–17289.
98. Kim, Y. C., Wikström, M., and Hummer, G. (2007) Kinetic models of redox-coupled proton pumping. *Proc. Natl. Acad. Sci. U.S.A. 104*, 2169–2174.
99. Wikström, M., and Verkhovsky, M. I. (2007) Mechanism and energetics of proton translocation by the respiratory heme-copper oxidases. *Biochim. Biophys. Acta 1767*, 1200–1214.
100. Bränden, G., Bränden, M., Schmidt, B., Mills, D. A., Ferguson-Miller, S., and Brzezinski, P. (2005) The protonation state of a heme propionate controls electron transfer in cytochrome c oxidase. *Biochemistry 44*, 10466–10474.
101. Brzezinski, P., and ädelroth, P. (2006) Design principles of proton-pumping haem-copper oxidases. *Curr. Opin. Struct. Biol. 16*, 465–472.
102. Busenlehner, L. S., Branden, G. S., Namslauer, A., Brzezinski, P., and Armstrong, R. N. (2008) Structural elements involved in proton translocation by cytochrome c oxidase as revealed by backbone amide and hydrogen-deuterium exchange of E286H mutant. *Biochemistry 47*, 73.
103. Popovic, D. M., and Stuchebrukhov, A. A. (2005) Proton exit channels in bovine cytochrome c oxidase. *J. Phys. Chem. B 109*, 3616–3626.
104. Riccardi, D., König, P., Prat-Resina, X., Yu, H., Elstner, M., Frauenheim, T., and Cui, Q. (2006) "Proton holes" in long-range proton transfer reactions in solution and enzymes: A theoretical analysis. *J. Am. Chem. Soc. 128*, 16302–16311.
105. Kato, M., Pisliakov, A. V., and Warshel, A. (2006) The barrier for proton transport in aqauporins as a challenge for electrostatic models: The role of protein relaxation in mutational calculations. *Proteins: Struct., Funct., Bioinf. 64*, 829–844.
106. Shurki, A., and Warshel, A. (2003) Structure/function correlations of proteins using MM, QM/MM, and related approaches: Methods, concepts, pitfalls, and current progress. *Adv. Protein Chem. 66*, 249.
107. Kato, M., and Warshel, A. (2006) Using a charging coordinate in studies of ionozation induced partial unfolding. *J. Phys. Chem. B 110*, 11566–11570.
108. Johansson, M. P., Kaila, V. R. I., and Laakkonen, L. (2007) Charge parameterization of the metal centers in cytochrome c oxidase. *J. Comput. Chem. 29*, 753–767.
109. Riccardi, D., Koenig, P., Guo, H., and Cui, Q. (2008) Proton transfer in carbonic anhydrase is controlled by electrostatics rather than the orientation of the acceptor. *Biochemistry 47*, 2369–2378.

BI8021284